Supplementary information for Near-zero environmental impact aircraft

Prakash Prashanth[1], Jad Elmourad[1], Carla Grobler[1], Stewart Isaacs[1], Syed Shayan Zahid[1], James Abel[1], Christoph Falter[1], Thibaud Fritz[1], Florian Allroggen[1], Jayant S Sabnis[1], Sebastian D Eastham[1], Raymond L Speth[1], Steven RH Barrett[1*]

[1]Laboratory for Aviation and the Environment,
Department of Aeronautics and Astronautics,
Massachusetts Institute of Technology, Cambridge MA, United States of America

S1. Present day environmental impacts due to aviation

The net monetized environmental (climate and air quality) impact of aviation in 2019 based on the OAG global flight schedule is estimated to be 410 billion USD per year. The total fuel burned by the fleet is 258 Tg. Therefore, the net monetized environmental impact is ~1600 USD/tonne of fuel burned. Climate related impacts account for 68% of these damages while degraded air quality accounts for the rest. Figure S1 shows the contribution of the emitted species to aviation's environmental impact. See section S9 and the Methods section of the main paper for details on the monetization approach taken.

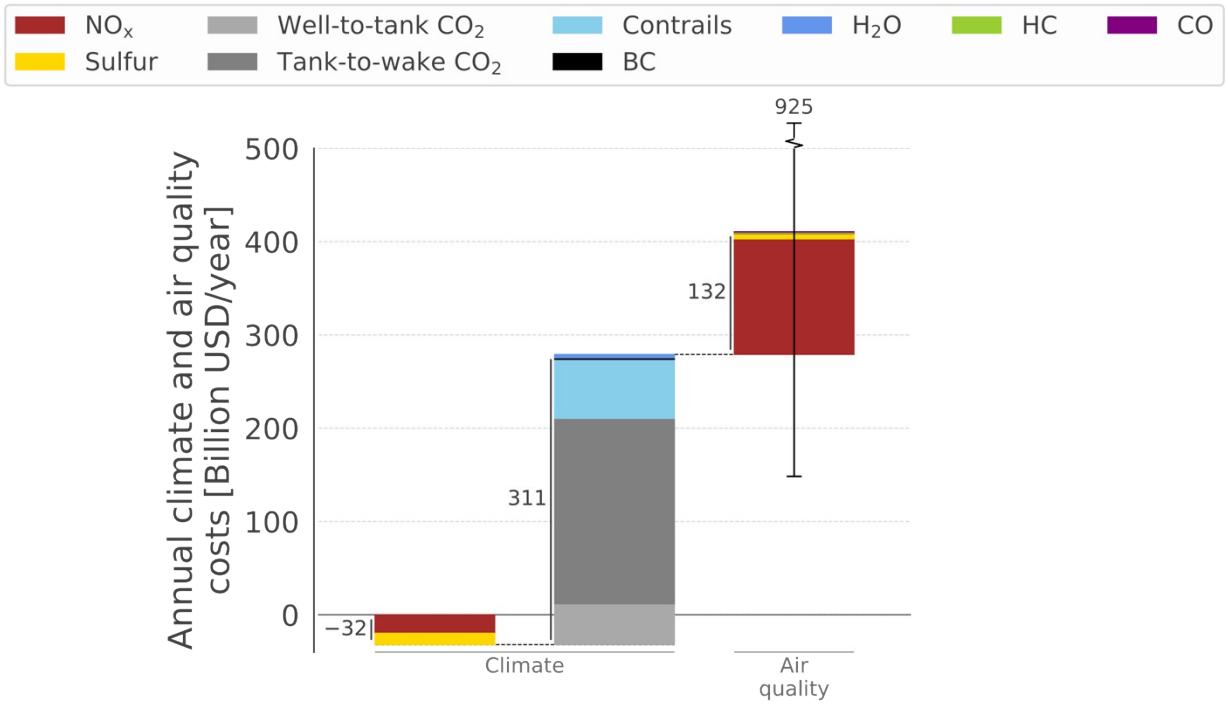

Figure S1: Annual environmental costs (air quality and climate) due to the civil aviation fleet in 2019

S2. Target aircraft class

Using the methods described in the Methods Section of the main paper and the 2019 OAG global flight schedule we find that civil aviation in 2019 burned 258 Tg of fuel. We find that 114 Tg (i.e., ~44%) of this fuel burn occurs on Boeing B737 and Airbus A230 family of aircraft on routes of less than 3000 nmi (see Figure S2) making this the most important segment for which to design zero-impact solutions. This, therefore, is chosen as our target market and an aircraft of 220 seats, 3000 nmi range, and cruise Mach number of 0.80 is used for our zero-impact aircraft design.

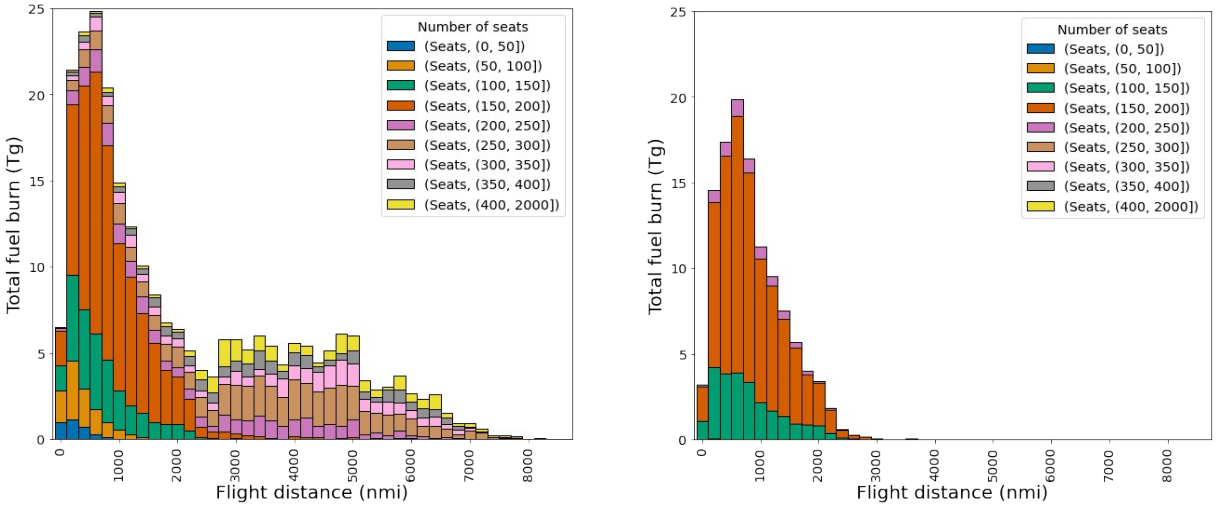

Figure S2: Fuel burn by flight distance, categorized by aircraft seat number. (a) shows all flights in the 2019 schedule data, while (b) shows only includes flights on Airbus 320 and Boeing 737 family aircraft on routes of less than 3000 nmi. These flights account for 44% of the total fuel burn.

S3. Present day environmental impacts of the target aircraft class

Figure S3 shows the present-day distribution of aviation's environmental impacts quantified for the target market segment. The net monetized environmental impact (consisting of air quality and climate impacts) attributable to the target market is ~177 billion USD per year. The net-climate impacts accounts for ~124 billion USD per year (~70% of the total) and the air quality impacts accounts for ~53 billion USD per year (30% of the total).

The components with the largest contribution are CO_2, contrails, and NO_x. CO_2 emissions account for 86% of the net climate impact and ~61% of the total environmental impact of aviation. Contrails account for 22% of the net climate impact and 16% of the total environmental impact. Note the sum of contrail and CO_2 impacts on climate are greater than 100% since aviation attributable aerosols result in a negative RF (cooling). Aviation emissions of NO_x account for ~96% of the air quality impact and 28% of the total environmental impact. We note that while the effective radiative forcing (ERF)* associated with contrails can be ~1.7 times[1] the RF due to aviation CO_2, the climate impact integrated into the future of CO_2 emissions is ~3 times the contrail related climate impact (see S1). This is due to the long atmospheric lifetime (hundreds of years) for CO_2 compared to contrails (which only last for several hours).
In addition to the above impacts, short-term forcers such as aviation attributable NO_x and SO_x have a negative radiative forcing (cooling), accounting for approximately −7.5% of the total environmental impact. Furthermore, black carbon (BC), unburnt hydrocarbons (HC) and carbon monoxide account for <2% of the net environmental impact.

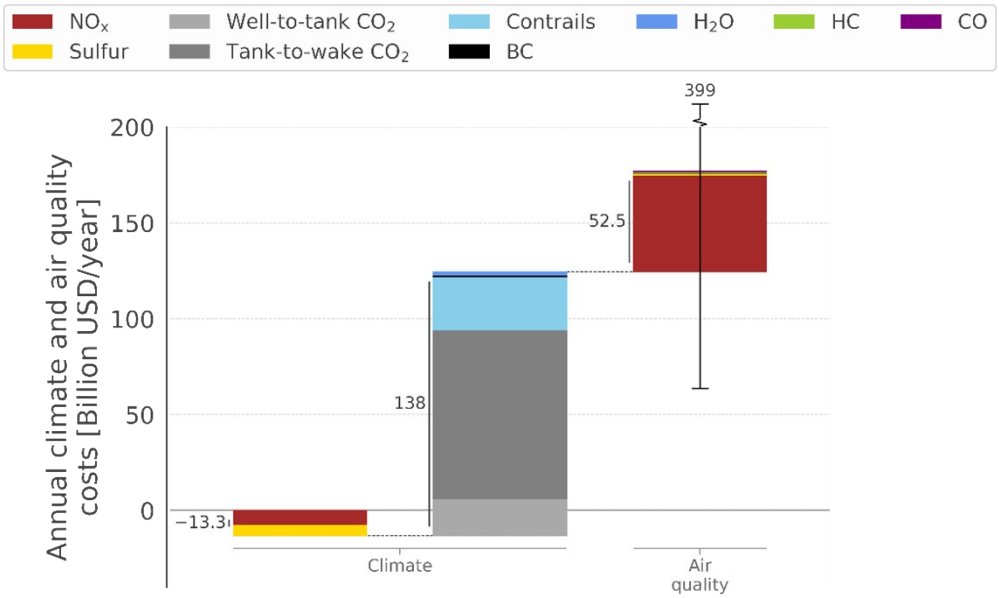

Figure S3: Monetized environmental impacts of present-day aviation in the market currently served by the Boeing 737 and Airbus A320 family. Error bars represent the 95% confidence interval of the total environmental impact.

* The instantaneous radiative forcing (RF) is calculated assuming the temperature of the atmosphere is held fixed everywhere, while the effective radiative forcing (ERF) allows the land and atmospheric temperatures to adjust to the new radiative forcing but assumes that the ocean conditions are held fixed. This is meant to capture the equilibration of all "fast" processes. See Lee et al [1] and Myhere et al [2] for further discussion.

S4. Life cycle costs and emissions from LH_2 and SAF production

The following tables outline the assumptions and inputs used to calculate the cost of fuel production and the lifecycle emissions associated with the production of the two fuels considered in this work. We assume the exclusive use of renewable electricity from solar and wind for the production and transportation of liquid hydrogen (LH_2) and power-to-liquid (PtL) fuel to minimize the lifecycle GHG emissions. The required electricity generation to support low-carbon fuel production for a fleet of ZIA aircraft (over 2000 TWh annually) is assumed to be developed for low-carbon fuel production purposes without grid integration, given the scale of required electricity.

Table S1 details the cost assumptions used under two technological lenses, an advanced technology lens that assumes rapid technological improvement between present day and 2050 and a moderate technology lens that assumes a slower pace of technological improvement. The levelized cost of electricity (LCOE) and capacity factors (CF) of utility scale photo-voltaic cells and on-shore wind energy are taken from the National Renewable Energy Laboratory (NERL) Annual Techonology Baseline (ATB) dataset [3] for the year 2050 assuming best available locations (Class 1) for both solar and wind energy.

Cryogenic LH_2 fuel necessitates changes to the infrastructure used for refuelling at airports. The choice of refuelling infrastructure depends on a particular airport's demand profile and layout. The fuelling costs used in this work are \$0.073 – \$0.084 per kg of hydrogen [4]. Approximately two-thirds of the annualized cost is associated with capital while operation costs account for the remaining third. The capital cost accounts for the cost of cryogenic hydrogen tanks, cryopumps, trucks, pipes, and dispenser capital costs. See Abel and Allrogen [4] for further details and breakdown.

As a comparison for Jet A prices and the total operating costs, data from the IATA [5] is used. Taking the Jet A price from 2004 to 2019 leads to an average price of 0.56 USD per L jet fuel with a standard deviation of 0.17 USD per L. Total non-fuel operating costs were found at 1.43 USD per L Jet A (standard deviation of 0.19 USD per L of fuel). These costs are combined and compared to the total operating cost of the ZIA aircraft by assuming only the fuel cost is sensitive to a change in fuel.

Table S1: Cost assumptions used in quantifying the fuel production pathway costs for expected year-2050 technology levels. LCOE is the levelized cost of electricity, CF is the capacity factor and O&M refers to the operating and maintenance costs.

			Units	Value		Source
				Advanced	Moderate	
Electricity generation	Photo-voltaic cells	LCOE	\$/kWh	0.010	0.017	NREL ATB [3]
		CF	%	37	33	

	On-shore wind	LCOE	$/kWh	0.010	0.020	
		CF	%	58	51	
Electrolyzer capital cost			$/kW	150	450	Mayyas et al [6]
CO_2 capture	Investment costs		$/tonne CO_2 /year	812	2170	Hanna et al [7]
	O&M costs		$/tonne CO_2	11.9	23.3	Hanna et al [7]
Fischer-Tropsch capital cost			$/kW	300	300	Falter et al [8]
Electricity transmission	Transmission line capital		millions of $/mile	2.3	9.3	Saadi et al and d'Amore-Domenech et al [9,10]
	Converter station		millions of $ per station	367.2	367.2	EIA [11]
Hydrogen fueling costs			$/kg	0.073	0.084	Abel and Allroggen [4]

Table S2 summarizes the energy demand associated with the various steps of the fuel production pathways considered here.

Table S2: Energy efficiency and losses in the fuel production processes steps for expected year-2050 technology levels.

Process	Component	Units	Value		Source
			Advanced	Moderate	
H_2 production	Electrolyzer efficiency	%	80	67	IEA [12]
CO_2 capture	Electricity demand	kWh/tonne CO_2	286	444	Hanna et al [7]
Liquefaction	Specific energy	kWh/kg	4.4	5.9	Aasadnia and Mehrpooya [13]
HVDC electric transport	Transmission loss	%	3.5	3.5	EIA [11]
	Conversion station loss	%	0.60	1.0	EIA [11]

Table S3 outlines the emission intensities of the fuel production processes. Emission intensities that are provided for 2020 in the literature are decreased by 50% to model a cleaner manufacturing value chain in 2050. This is consistent with the approach taken in the ICAO Report on the feasibility of a long-term aspirational goal (LTAG) for international civil aviation CO_2 emissions reduction [14].

Table S3: Emission intensities of electricity generation and other processes, including embodied emissions. All values that were provided for 2020 or earlier have been reduced by 50% relative to the indicated sources to estimate the emission intensity in 2050 to account for decarbonization in the manufacturing value chain. DAC plant embodied emissions shown are for with or without material recycling as reported by Deutz and Bardow [15].

Process		Units	Value	Source
Electricity generation	Photo-voltaic cells	gCO_2e/kWh	22	Kim et al [16]
	On-shore wind	gCO_2e/kWh	2.2	Razdan and Garrett [17]
Electrolysis	PEM embodied emissions	gCO_2e/kgH_2	60	Bareiß et al [18]
Liquefaction	Liquefaction plant embodied emissions	gCO_2e/kgH_2	50	Assumed similar plant embodied emissions as Fuel conversion
CO_2 capture	DAC adsorbent emission intensity	$gCO_2e/kgCO_2$ captured	13	Deutz and Bardow [15]
	DAC plant embodied emissions	$gCO_2e/kgCO_2$ captured	[3.0, 8.0]	
Fuel conversion	Fischer-Tropsch and rWGS embodied emissions	gCO_2e/L jet fuel	30	Falter et al [8]
Electricity transport	HVDC construction embodied emissions	gCO_2e/kWh	1.25	Arvensen et al [19]

The calculated total electricity demand for each pathway is detailed in Table S4. The LH_2 pathway has a ~32% lower electricity demand per unit fuel energy (LHV basis) than the production of PtL SAF. Given the lifecycle emissions intensity of wind electricity assumed here (see Table S3) of 2.2 gCO_2e/kWh (= 0.61 gCO_2e/MJ), electricity demand accounts for ~1 gCO_2e/MJ fuel energy for LH_2 (and 1.5 gCO_2e/MJ fuel energy for the PtL-SAF.

Table S4: Derived mean electricity demand (LHV basis) for each fuel production pathway. Electricity demand for production of hydrogen in the LH_2 pathway also accounts for the transmission losses incurred during the HVDC transport of electricity and AC/DC conversion.

	Units	**Production of gaseous H_2**	**Liquefaction**	**Total**
LH_2	kWh/MJ	0.41	0.043	0.46
	MJ/MJ	1.49	0.15	1.64
	Units	**Production of gaseous H_2**	**DAC of CO_2**	**Total**
PtL-SAF	kWh/MJ	0.64	0.037	0.68
	MJ/MJ	2.30	0.13	2.43

S5. Aircraft design

A multi-disciplinary design and optimization approach derived from the Transport Aircraft System Optimization (TASOPT) [20,21] code is adopted to design and optimize the aircraft for the target market (3000 nmi range, 220 passengers and cruise Mach number of 0.8). Use of non-traditional configurations such as the D8 lifting fuselage and cruise Mach number reductions could result in further performance improvements [21] but are not the focus of this work. (This is on the basis that the introduction of PCEC and a turboelectric powertrain, potentially along with a cryogenic fuel, is already a huge technological step that is unlikely to be combined with unconventional configurations. Furthermore, the potential scale of impact of fuel lifecycle, contrail avoidance, and PCEC on environmental impacts is significantly greater than aerodynamic and aerostructural improvements – although those will remain important.) The overall configuration of both aircraft is chosen to be a tube-and-wing design. This allows the use of 2D viscous/inviscid coupled CFD and structural sizing based on beam bending theory. The following sections detail the models used for the aircraft components.

S5.1. Design of cryogenic liquid hydrogen tanks

The zero-impact aircraft (ZIA) system fueled by liquid hydrogen (LH_2) needs an aircraft design that is compatible with the LH_2 fuel. LH_2 has ~2.73 times the specific energy relative to Jet A (120 MJ/kg vs 43 MJ/kg for Jet-A/ SAF) but only has ~25% of volumetric energy density of Jet A. The storage of cryogenic hydrogen in aircraft, therefore, presents unique challenges due to the low volumetric energy density. Liquid hydrogen is more likely to permeate through the fuel container walls, presenting an additional design challenge [22]. Appropriate insulation is also required to ensure acceptable boil-off rates.

Due to its low density [23], foam-based insulation is assumed in this analysis. Brewer [24] recommended a foam-based insulation configuration in which the inner metal wall of the tank is enclosed by two layers of foam separated by a vapor barrier to prevent permeation between the layers. A composite fairing applied on the outer wall of the tank, separated from the foam layer by another vapor barrier, prevents damage from the surroundings as shown in Figure S4 below.

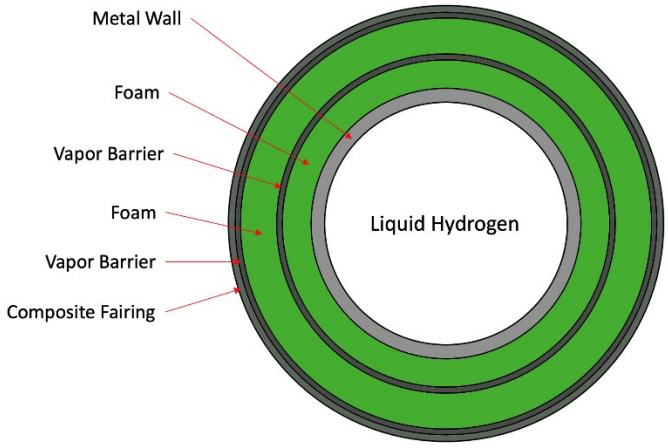

Figure S4: Cross-sectional illustration of the cryogenic liquid hydrogen tank

The key requirement for the structural metal wall is to be as lightweight as possible while having a high yield strength to withstand the load. Furthermore, the tank wall must not be prone to embrittlement while in contact with the LH_2. Aluminum 2219 alloy is chosen for its low density and high strength characteristics with a limited stress of 172.4 MPa under ultimate design conditions, as well as a density of 2825 kg/m^3 at a cryogenic temperature of 20 K. The insulating material needs to have a low thermal conductivity, good mechanical strength, and light weight. A polymethacrylimide foam (Rohacell) satisfies these criteria with a density of 35.24 kg/m^3 and a thermal conductivity $k,$ between 5 and 35 mW/mK depending on the temperature and is used in this analysis. A multilayer sandwich consisting of a Mylar layer, followed by two Aluminium layers, another Mylar layer, and a polymer (Darcon) or glass net fabric (MAAMF), is used as the vapor barrier between the foam and fairing layers [23]. The MAAMF vapor barrier used in this configuration has a surface density of 0.225 kg/m^2 with a thickness of ~0.015 mm. Finally, the composite fairing applied on the outside has a surface density of 1.304 kg/m^2 with a thickness of ~16 mm.

The aluminum wall of the tank is sized using standard pressure-vessel analysis. In this analysis, a 1.5 bar pressure difference is assumed across the walls of the pressure vessel. A factor of safety of 2 is applied to make the tank burst-resistant [24], which is consistent with the ASME Boiler and Pressure vessel code, used by Barron [25]. A 10 cm clearance from the fuselage, and a weld efficiency η_{weld} of 90% to account for weld joints in the tank is assumed. An ullage allowance of 10% by volume of fuel [25] is assumed.

In order to estimate the hydrogen boil-off rate from the tank, a thermal resistance model is used to calculate the rate of heat transfer between the liquid hydrogen and the ambient. An additional heat transfer factor of 1.3 is multiplied to the heat transfer rate to account for heat leaks from pipes and valves [26].

S5.2. Loss models in electric machines

Figure S5 illustrates the permanent magnet electric machines used to model the electric motors and generators.

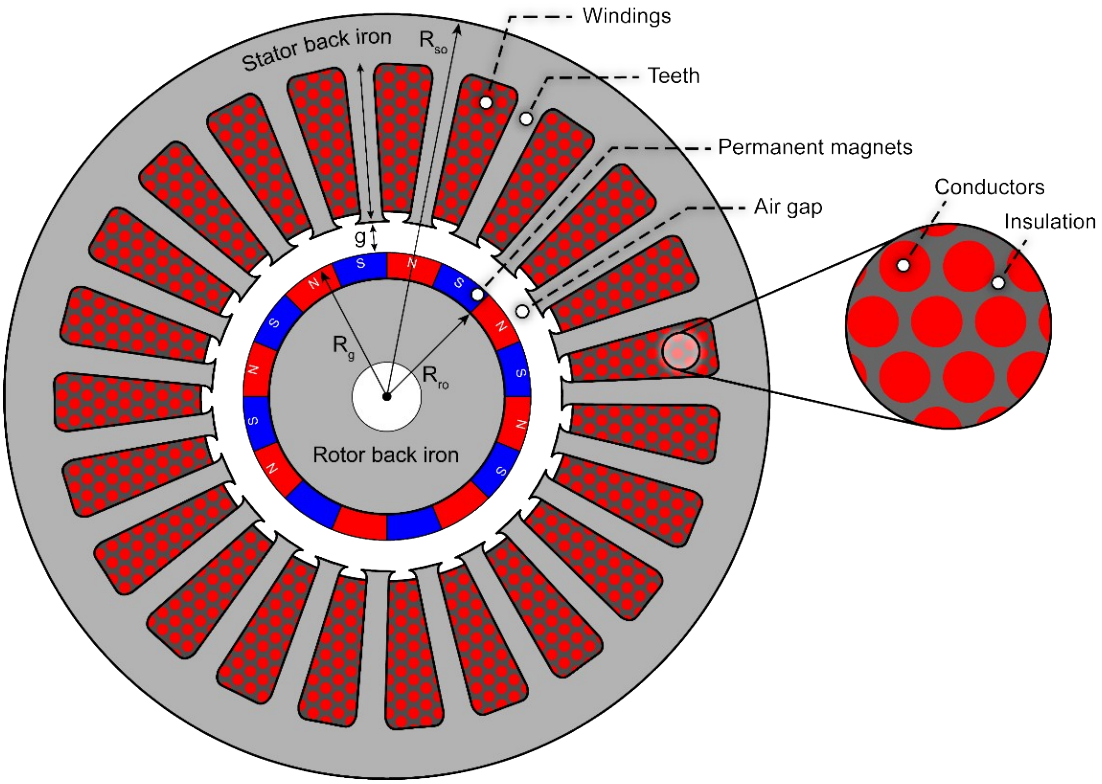

Figure S5: Schematic of permanent-magnet electric machines used in this work.

The rotor of the electric machine is sized based on the maximum tip speed of the rotor, which is limited to 250 m/s and a rotor angular speed determined from the shaft speed. A simplified magnetic circuit [27] is used to determine the magnetic flux density in the air gap for a given air gap thickness the rotor and stator back iron are subsequently sized such that the magnetic flux density does not exceed the saturation flux density of the material. The laminations are assumed to be made from M-19 steel. The efficiency of the machine is calculated by accounting for core losses (due to eddy currents and hysteresis), windage loss in the rotor and ohmic losses in the conductors.

The efficiency of the motor is calculated by quantifying the losses in the machine for any given operating condition. The total loss is the sum of the windage loss in the air gap, the ohmic loss in the conductors and the core losses in the ferromagnetic material. The windage loss is calculated using the air gap Reynolds number and average turbulent friction coefficient in the air gap by using a flat plate flow approximation. The core losses are comprised of the hysteresis losses in the ferro-magnetic material and the eddy current losses in the teeth, rotor, and stator back iron. The core losses are modeled using the Steinmetz equation with empirical coefficients which were derived based on data [28]. The core losses are sensitive to the material properties as

detailed below. The ohmic losses in the armature windings are calculated assuming copper wires and a prescribed armature temperature of ~90°C. The loss models used to calculate the performance of the variable speed generator and motor used in the power train are summarized in the Table S5 below.

Table S5: Loss models used to estimate the performance of the permanent magnet electric machines.

Loss component	Physical loss process	Model
Windage loss	Power lost due to fluid viscosity in the air gap	$Q_{wind} = C_f \times \pi \rho_{air} \omega^3 R_g^4 \times l_{stk}$
Ohmic loss	Power dissipated in the conductors through electrical resistance	$Q_{ohmic} = I^2 \times (2R_{ph})$
Core loss	Power dissipated in the iron through hysteresis and eddy currents modeled by the Steinmetz equation	$Q_{core} = m_{sbi}\left(k_e f^2 B_{sbi}^2 + k_h f B_{sbi}^{\alpha}\right) + m_{teeth}\left(k_e f^2 B_{teeth}^2 + k_h f B_{te}$

The key difference in modeling the generator and the motor is in power conversion – the generator converts mechanical shaft power to electrical power while the motor converts electrical power into mechanical shaft power. These are calculated as follows:

$P_{gen,elec} = P_{gen,\ shaft} - Q_{gen,total}$,

$P_{mot,shaft} = P_{mot,\ elec} - Q_{mot,total}$,

where $P_{gen,elec}$ and $P_{mot,\ elec}$ are the generator and motor electrical power, $P_{gen,\ shaft}$ and $P_{mot,\ shaft}$ are the generator and motor shaft power and Q is the total power loss in the respective electric machines.

The core losses of the machine can be further reduced by using state-of-the-art materials such as Vacoflux48 or Hiperco20 which could significantly reduce the core losses relative to M19 steel. Higher torque densities could also be achieved due to the higher saturation flux density of Vacoflux48 of 2.0T that could result in a smaller, torque dense machine.

S5.3. Turbo-electric powertrain

Figure S6 shows a schematic of the turbo-electric powertrain. The aircraft are powered by two gas turbine engines located in the aft section of the fuselage. Each gas turbine delivers shaft power to two variable speed electrical generators which use a rectifier to convert the alternating current (AC) to a direct current (DC) output for transmission. Use of two generators per gas turbine core provides redundancy while allowing each generator to be sized for a cruise power of ~2.5 MW (see Table S6 for peak power). The DC transmission cables are sized following existing methods [29]. The DC power is converted to AC by inverters that power the electrical motors located on the wing of the aircraft. The electrical motors provide shaft power to low pressure ratio podded propulsors. Each gas turbine also powers boundary layer ingesting ducted fans via an epicyclic gearbox that are integrated into the aircraft fuselage. A thermal management system is required to remove waste heat from the system for both aircraft. For ZIA-LH_2 the cryogenic fuel is used to cool the variable speed generators located at the aft of the aircraft (that are in proximity to the LH_2 fuel tanks and the gas turbine where the fuel will be burned) while the motors and inverters located on the wing require an active thermal management system. All waste heat due to electrical components in the ZIA-SAF is assumed to be removed by an active thermal management system.

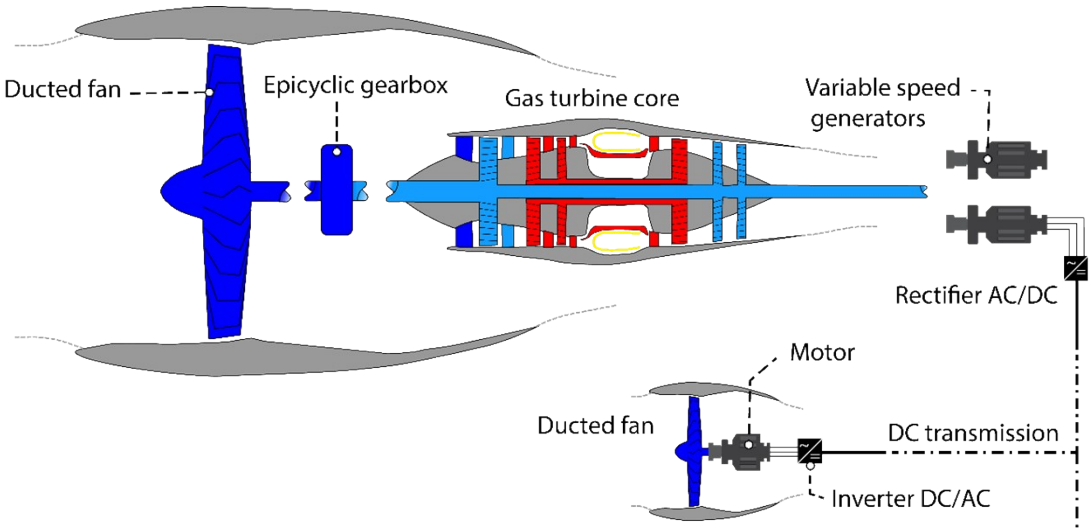

Figure S6: Turbo-electric powertrain schematic. Exhaust gases from the gas turbine core is fed into the post-combustion emissions control system (not shown). The larger ducted fans are integrated into the aft section of the fuselage while the smaller podded propulsors are distributed across the wings.

Component weights are analytically calculated for the electric generators and motors. The weight of the nacelles and ducted propulsors are calculated using the semi-empirical methods in TASOPT [21] and Sagerser et al [30]. A simplified weight model following Hall et al [29] is used to calculate the weight of the gas turbine core while the inverters and rectifiers are assumed to have a specific power of 19 kW/kg in line with on-going projects [29,31]. The thermal management systems are assumed to have a specific power of 13 kW/kg [29]. Table S6 summarizes key performance metrics of the powertrains for both the ZIA-SAF and the ZIA-LH_2.

Table S6: Powertrain performance details for ZIA-SAF and ZIA-LH_2. Design point values are specified unless otherwise stated.

	ZIA-SAF	ZIA-LH_2
Generator		
Design power [kW]	2350	1500
Peak power [kW]	4430	2670
Specific power [kW/kg]	10.7	10.6
Design efficiency [%]	97.0	97.0
Ohmic loss [kW]	4.10	2.81
Windage loss [kW]	7.60	4.70
Core losses [kW]	59.2	37.8
Shaft length [m]	0.45	0.29
Diameter [m]	0.37	0.37
Motor		
Design power [kW]	1080	700
Peak power [kW]	2100	1260
Specific power [kW/kg]	9.80	9.52
Design efficiency [%]	97.3	97.3
Ohmic loss [kW]	2.50	1.85
Windage loss [kW]	3.22	1.99
Core losses [kW]	23.8	15.2
Shaft length [m]	0.20	0.13
Diameter [m]	0.40	0.40
Gas turbine core and fans		
$\pi_{fan,aft}$	1.30	1.30
π_{LPC}	3.0	3.0
π_{HPC}	11.8	12.7
OPR	46.0	49.5
Thermal efficiency [%]	50.2	52.4
Core thrust fraction [%]	2.5	2.8
Aft fan thrust fraction [%]	39.5	65.4
Wing mounted fans thrust fraction [%]	58.0	31.8
Core size [kg/s]	1.09	1.40
Core size [lbm/s]	2.40	3.08
Core physical mass flow [kg/s]	11.1	14.7
Core physical mass flow [lbm/s]	24.6	32.4
Aft fan diameter [m]	1.78	2.45
Wing mounted fan diameter [m]	1.10	0.88
Catalyst		
Cell density [cells per square inch]	900	900
Cell wall thickness [m]	5.08e-5	5.08e-5
Frontal flow area [m^2]	7.27	11.2
Reacting channel length [cm]	1.25	1.25
Gas residence time [ms]	1.70	2.20
deNOx at design point [%]	99.0	99.0
deNOx at takeoff [%]	93.4	94.0
Catalyst Damköhler number, Da	1700	1500
Total weight of PCEC systems [N]	2450	2760

S5.4. Post combustion emissions control

The post-combustion emissions control system is designed based on Prashanth et al [32] and is summarized here. A selective catalytic reduction approach is used with anhydrous ammonia (NH_3) sprayed upstream of the catalyst. The lumped parameter model [33] shows that the efficiency of NO_x removal in the catalyst is a function of the local Sherwood number $Sh(z^*)$ and Damköhler number (Da),

$$deNO_x = 1 - \exp\left(-4\int_0^{z^*}\frac{Da \times Sh}{Da + Sh}dz^*\right),$$

where $z^* = (zD_{NO})/(ud^2)$, D_{NO} is the diffusion coefficient of NO, z is the axial distance along the catalytic channel, u is the local flow velocity and d is the hydraulic diameter of the channel. The Damköhler number is defined as the ratio of the rate of chemical reaction at a catalytic site to the mass transfer rate,

$$Da = \frac{k_c d}{D_{NO}},$$

$$k_c = \sqrt{k_{NO} D_{eff,NO}},$$

where k_c is the effective reaction rate, $k_{NO} = 1.28 \times 10^{11}\exp\left(-\frac{22400}{RT}\right) s^{-1}$ is the chemical reaction rate [34] at the catalytic site in units of s^{-1}. $D_{eff,NO}$ is the effective diffusion of the gases through the catalytic wash coat. Figure S7 shows the $deNO_x$ as a function of non-dimensional distance z^*, there is little variation in performance for $Da > 100$.

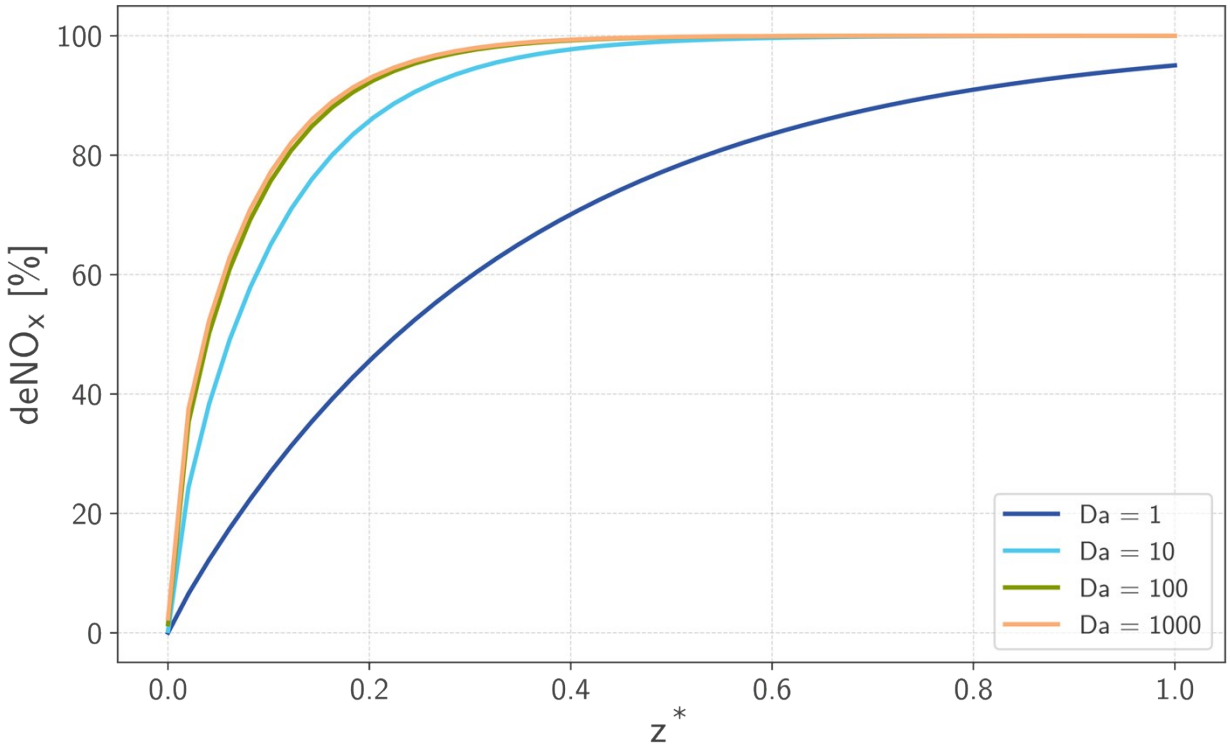

Figure S7: $deNO_x$ versus non-dimensional distance z* for different Da.

S5.5. Resulting aircraft design

The LH_2 and SAF aircraft obtained using the multi-disciplinary design optimization outlined above are shown in Figure 1 of the main text. Figure S8 and Figure S9 below show the weight buildup of both the LH_2 and SAF aircraft.

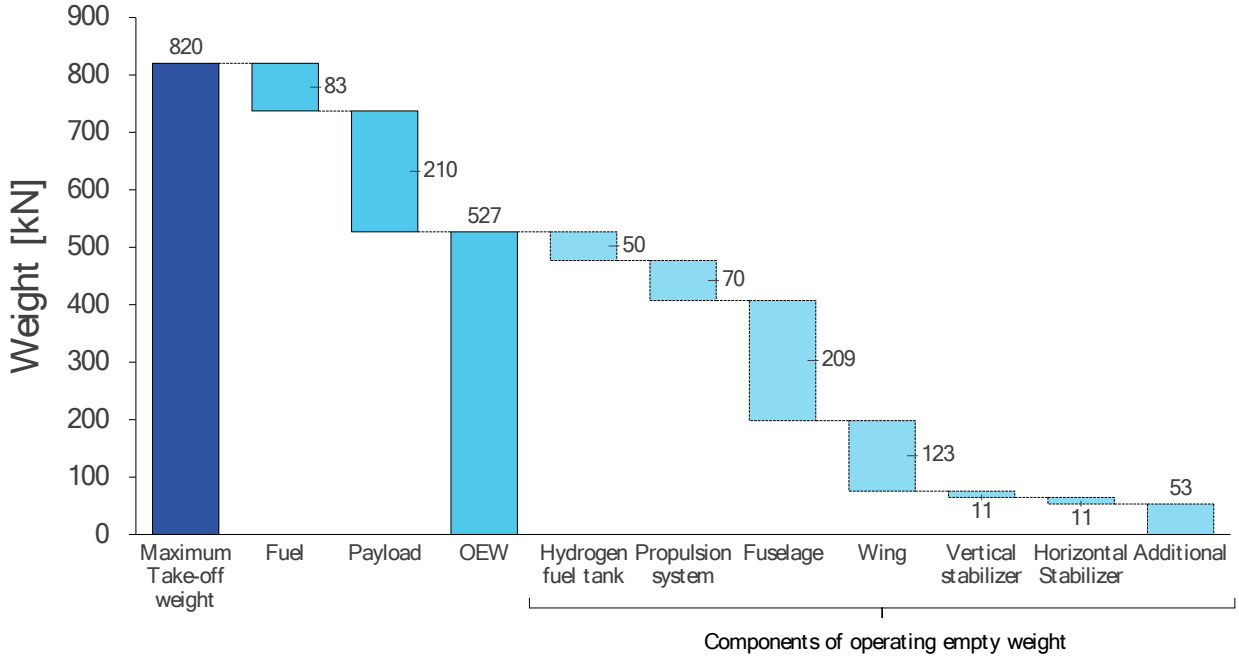

Figure S8: Weight build-up for the LH_2 fueled aircraft in kN. Additional weight includes weight of the landing gear, the hydraulic and pneumatic systems.

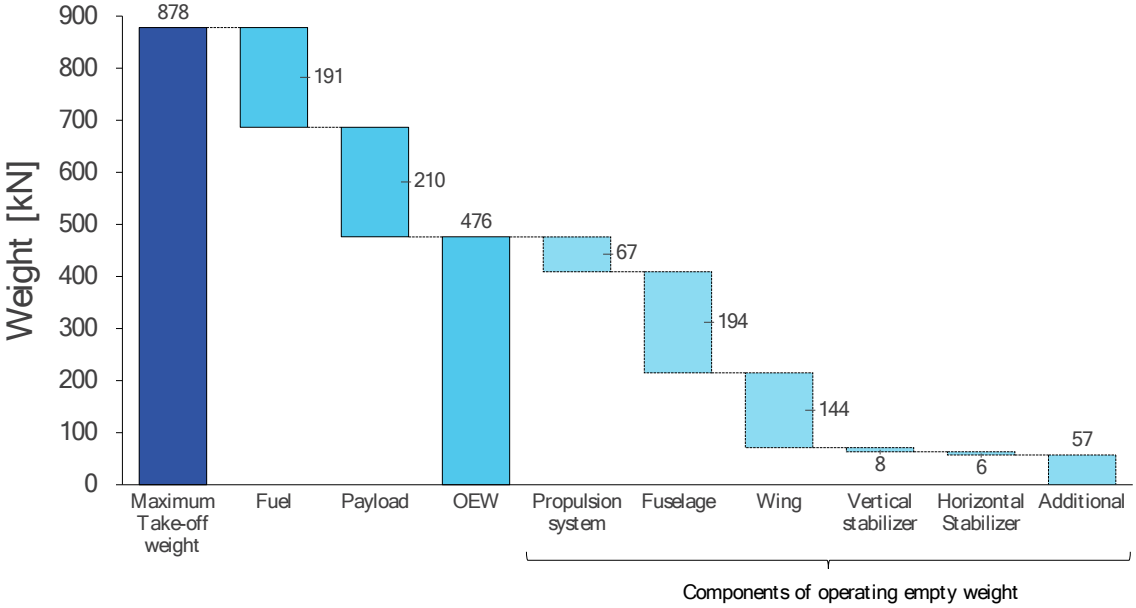

Figure S9: Weight build-up for the SAF fueled aircraft in kN. Additional weight includes weight of the landing gear, the hydraulic and pneumatic systems.

The operating empty weight (OEW) of the ZIA-SAF is 22% higher than for an optimized Boeing 737-800 [20] without PCEC due to the change in configuration (increased wingspan, turbo-electric powertrain, thermal management system, PCEC components). The fuel weight of the ZIA-LH_2 is ~43% of the fuel weight of the ZIA-SAF and is the reason the MTOW of the ZIA-LH_2 is lower than the ZIA-SAF. The operating empty weight (OEW) of the LH_2 aircraft is ~11% higher than the SAF aircraft primarily due to the cryogenic LH_2 tanks. The turbo-electric power train in both aircraft is ~32% larger than the two LEAP-1B power plants on the Boeing 737-MAX. The mass of the post-combustion emissions control systems (including the catalyst and auxiliary systems such as ammonia storage tanks, pumps etc.) are estimated to be 280 kg for the ZIA-LH_2 and 250 kg for the ZIA-SAF. A tube and wing configuration was chosen for both aircraft as shown in Figure 2 of the main text. A double-bubble fuselage like the D8 could result in additional performance benefits through secondary effects enabled by the lifting double-bubble fuselage.

Figure S10 below shows the drag areas of the ZIA-LH_2 and ZIA-SAF. The overall drag area of the ZIA-LH_2 is ~20% larger than that of the ZIA-SAF – the larger fuselage of the ZIA-LH_2 required to accommodate the LH_2 tanks increases the fuselage drag area by ~50%. The ZIA-SAF aircraft has a lift-to-drag (L/D) ratio of 19 which is ~27% higher than the ZIA-LH_2 (L/D = 15) and ~19% higher than that of an optimized 737-800 [20] (L/D = 16) primarily due to the increased wingspan. The lack of wing bending relief due to the absence of fuel in the wings of the ZIA-LH_2 results in increased wing root bending moment that leads to smaller aspect ratio wings relative to the ZIA-SAF (which benefits from wing bending relief due to fuel stored in the wings). This leads to a ~28% increase in induced drag for the ZIA-LH_2 relative to the ZIA-SAF.

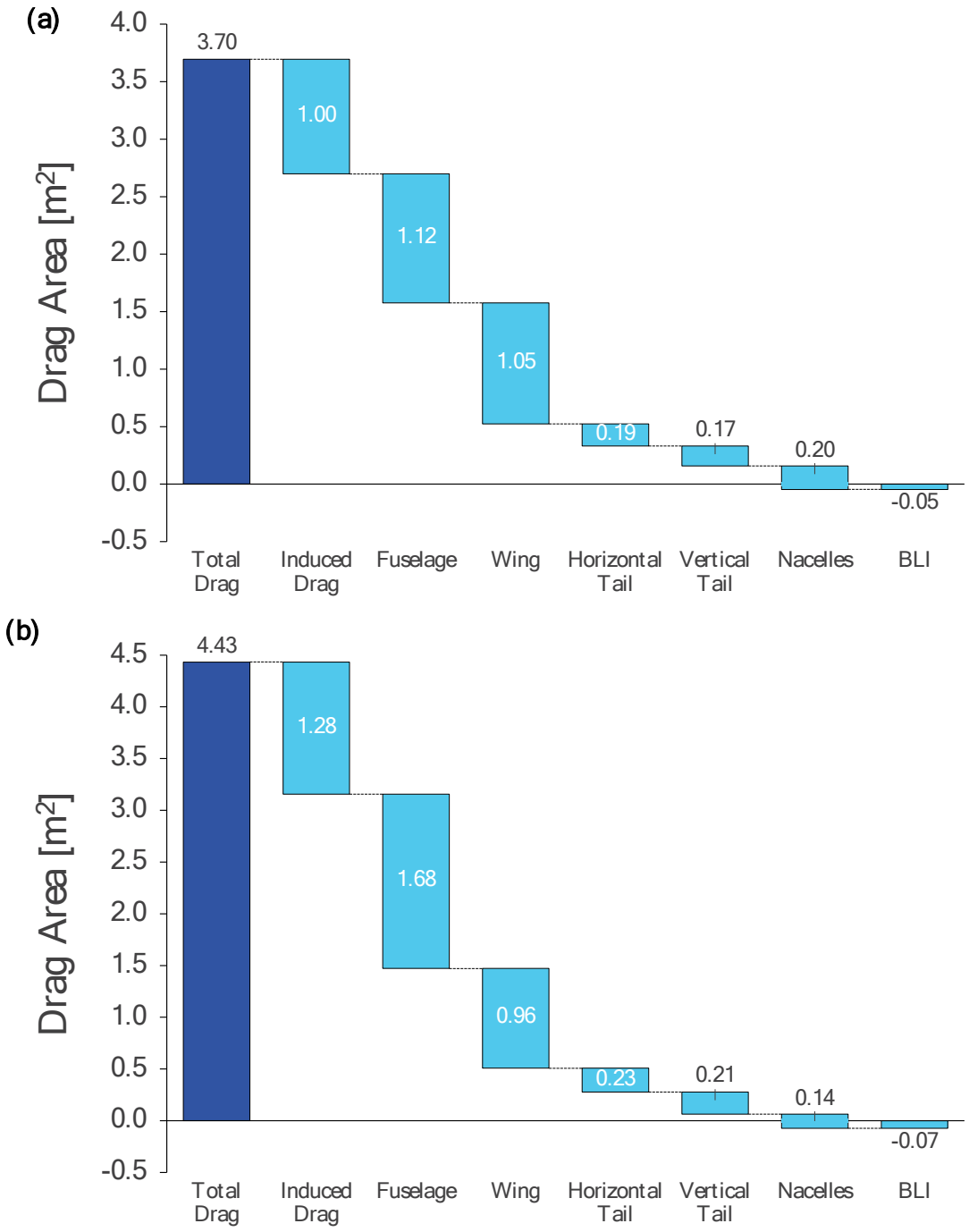

Figure S10: Drag area of (a) ZIA -SAF and (b) ZIA-LH_2 . The drag areas are computed as the product of the drag coefficient C_D and the reference area S_{ref}.

S6. Contrail avoidance

In our contrail avoidance simulations, we constrain the maximum fuel burn penalty of contrail avoidance for any flight to be no larger than 5% relative to the same mission without contrail avoidance. A Uniform-Cost Search algorithm is used to minimize the cost function below,

$$\text{cost} = (\text{contrail length}) \times \alpha + (\text{fuel burn}) \times (1 - \alpha),$$

where α is a trade-off parameter that varies between 0 and 1, indicating the relative weighting between contrail length and fuel burn. It uses a weighted graph with different costs (i.e., weights) along the edges to find the lowest-cost path between two nodes on the graph. The airspace between the two airports is discretized into a two-dimensional grid. One dimension is the altitude discretized by flight levels at 2000 ft intervals. The other dimension is the distance travelled from the origin airport along the great circle path, with the discretization set to 250 nautical miles. Although the airspace is discretized to only two dimensions, the nodes on the graph include an additional dimension. Each node is characterized by (1) the aeroplane's altitude, (2) its distance from the origin airport taken along the great circle path, and (3) the aeroplane's gross weight. A similar approach was taken by Gao and Hansman [35].

The contrail length estimates for any given flight are determined based on data from the ERA5 dataset provided by the European Centre for Medium-Range Weather Forecasts. Aircraft performance metrics are calculated using the aircraft design and optimization tool described above and in the main paper. In addition, we obtain the engine exhaust temperature and the fuel-to-air ratio to be used for the PCC calculation. The airplane design introduces an altitude ceiling above which the airplane cannot operate (assumed to be the altitude where the climb rate is less than 100 ft/min), and that limit is accounted for in the contrail avoidance simulation. The total fuel capacity of the aircraft is used to limit the maximum fuel that can be used for contrail avoidance.

We simulate our contrail avoidance by randomly sampling flights from the 2019 global flight schedule, for flights that were operated by the Boeing 737 or the Airbus A320 family of aircraft. The flight schedule accounts for ~23 million flights. Random sampling is continued until the values for fleet-wide contrail length reduction and the fleet-wide fuel burn penalty converge. We could that our results converged when the sample size approached ~3000 unique flights. The sample values are then generalized to the fleet. The fleet-wide fuel burn penalty is calculated by dividing the sample's total fuel burn when performing contrail avoidance by the sample's total fuel burn without contrail avoidance.

Figure S11 shows the reduction in contrail length (as a percentage of total distance flown) from the baseline trajectory (without contrail avoidance) as a function of the increase in fuel burn required to fly the modified trajectory.

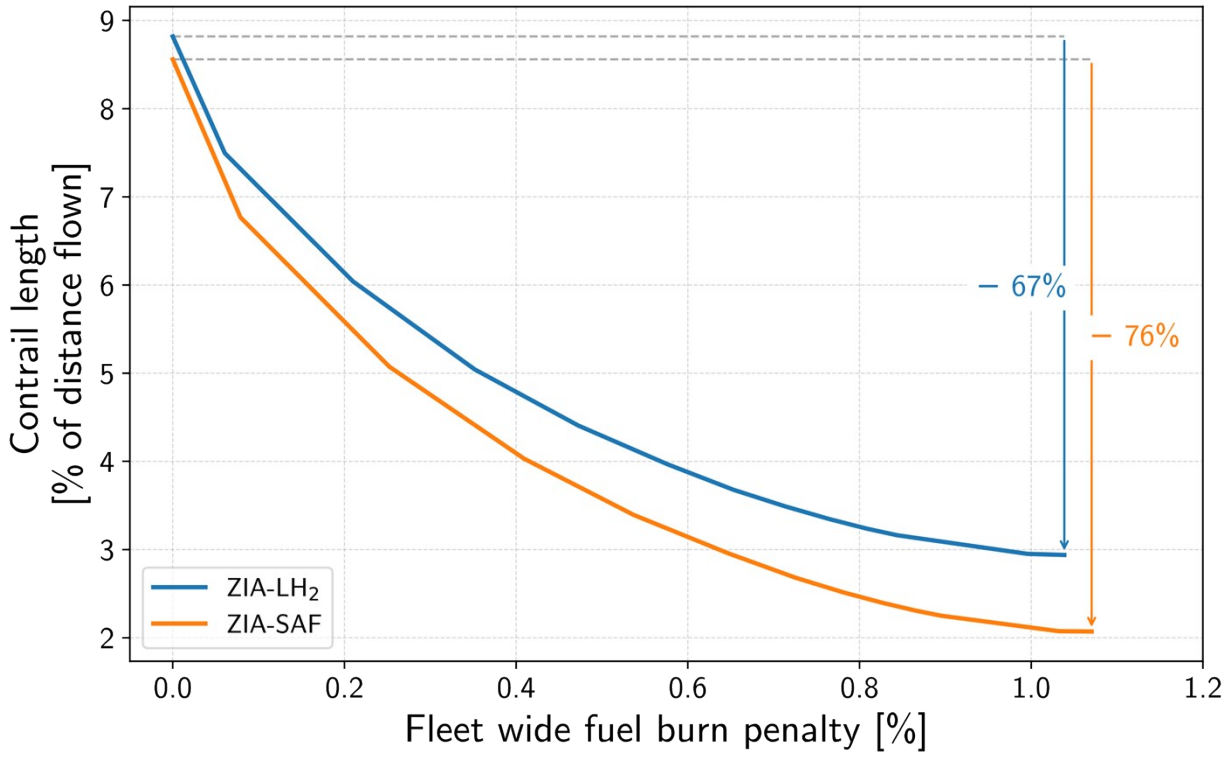

Figure S11: Contrail avoidance trade-off between contrail length and additional fuel burn for ZIA – LH_2 and SAF designs while constraining the maximum fuel burn penalty for any individual flight to be <5% (relative to the same mission without contrail avoidance. The fleet average contrail length is shown as a percentage of the total fleet average distance flown, while the fuel burn increase is the fleet average increase in fuel relative to a scenario where no contrail avoidance is performed.

Results in Figure S11 and the Main paper are for a constrained case where the fuel penalty incurred by any individual flight is no greater than 5%. The reduction shown above is measured from each design's respective baseline contrail length that would be formed if no contrail avoidance were to be used. Without contrail avoidance, the ZIA-SAF forms contrails over 6.6% of the distance flown, whereas ZIA- LH_2 forms contrails over 8.2%. With contrail avoidance, the contrail length drops to 1.8 % and 2.7% of the distance flown for ZIA-SAF and ZIA- LH_2 respectively. The fleet-wide fuel burn penalty associated with the above contrail avoidance is less than 1.0% for both ZIA-SAF and ZIA- LH_2. This represents the additional fuel required by the entire fleet, including flights that do not form contrails or perform contrail avoidance.

Considering only the section of the fleet that performs contrail avoidance, the averaged fuel burn penalty is 2.1% for both ZIA-SAF and ZIA-LH_2, while the maximum fuel burn penalty incurred by an individual flight is 16% for ZIA-SAF and 13% for ZIA- LH_2. See S9.2 for details on how contrail RF is estimated for the use of LH_2 and SAF. Further optimization using an objective function of contrail forcing rather than contrail length is also possible, which would result in lower tradeoffs. However, given the fuel penalty is only ~1% and we are addressing the full aircraft-energy-operational lifecycle this further optimization is considered more appropriate to specialized studies. This also allowed for broader comparison with the literature to add confidence to our estimate.

S6.1. Sensitivity to baseline trajectory

In our contrail avoidance simulations, we quantify the effects of rerouting aeroplanes above or below regions of the atmosphere where contrails are expected to form and persist. Specifically, we consider the contrail length reduction and the fuel burn penalty, which are both measured as a percentage relative to the baseline. The choice of the baseline influences the interpretation of the results, as it can either magnify or reduce the relative changes. Our baseline trajectory is a vertically wind-optimized trajectory that is laterally fixed to the great circle route. The wind-optimized baseline takes advantage of tailwinds to reduce the mission fuel burn.

However, flights deviate from the great circle path due to air traffic congestion or to avoid areas of turbulence or to reduce flight time and fuel burn by making use of strong tailwinds. Therefore, we evaluate the sensitivity of our results to the choice of the baseline lateral route by using real flight track data collected from Automatic Dependent Surveillance-Broadcast (ADS-B) via the OpenSky database. We compare the contrail length, contrail length reduction, and fuel burn penalty from two contrail avoidance simulations run on the same set of flights. One simulation extracts the lateral route from the ADS-B data, while the other uses the great circle route. In both simulations, the lateral route is fixed when performing contrail avoidance, and only altitude changes are applied. We use our ZIA-SAF design in this comparison study and find a <0.1% difference in the fuel burn penalty, and 0.4% difference in the contrail length reduction.

S6.2. Comparison with other literature

The contrail avoidance trade-off presented here is comparable to results from other studies [36–40]. Most of these studies include lateral diversions as part of their contrail avoidance strategy. This allows for a greater contrail length reduction but with higher fuel burn penalties. Furthermore, some of these studies are limited in the number of flights considered and in their geographical, seasonal, and diurnal distributions. By taking a random sampling approach (see Methods) our contrail avoidance simulation provides more confidence in generalizing our trade-off results and applying them to the entire global fleet.

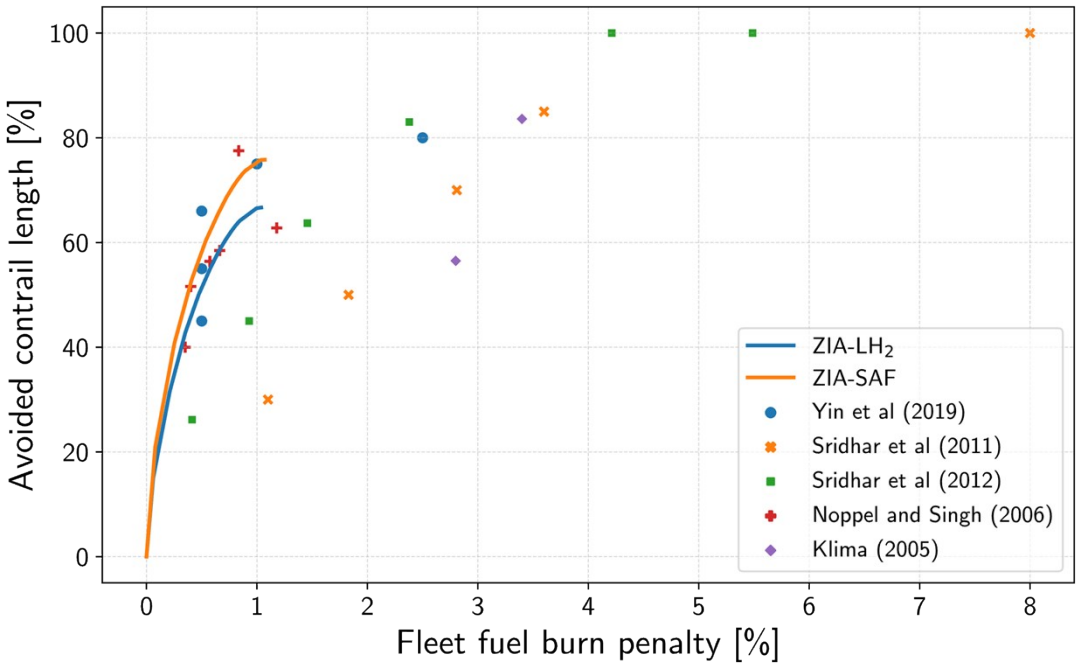

Figure S12: Comparison of contrail length reduction and fuel burn penalty tradeoff with existing literature.

S7. CO_2 capture and storage

Direct air capture (DAC) of CO_2 is used as a source of carbon in the Power-to-Liquid (PtL) sustainable aviation fuel (SAF) production pathway as it has no known adverse air quality impacts [41] assuming the use of clean electricity. Additionally, DAC is also used to capture atmospheric CO_2 to reach net-zero climate impact by addressing the residual emissions in the ZIA systems that are prohibitively expensive to avoid – residual lifecycle emissions in the fuel production and contrails that are infeasible to avoid.

We assume that the DAC plants are powered by renewable electricity (see Section S4) with the same assumptions used as in the fuel production. Given the investment and operating costs outlined in Section S4, we estimate the cost DAC is between $112 and $341 per tonne of captured CO_2 using wind powered electricity. Note that while we use the baseline investment cost form literature the costs are calculated using a consistent LCOE, CF, and WACC.

We additionally use a transportation cost [42] of ~18-30 $/tonne of CO_2 and a storage cost of ~$8 per tonne of CO_2 stored in geological formations per the IPCC Special Report on CCS [42].

The storage deployment potential for CO_2 in geological formations in 2050 is estimated to be 5 $GtCO_2$ (5000 Tg) per year [42]. Storage in geological formations is also likely to retain 99% of the stored CO_2 for over 1000 years [42] making DAC with storage effective in offsetting the residual climate impacts from the ZIA system.

We also note that the theoretically available storage capacity for CO_2 is likely between 8,000 and 55,000 $GtCO_2$ [43] which exceeds the estimated storage requirements under the IEA Sustainable Development Scenario over the period 2020 – 2070 [44]. However, the costs associated with the scale up of storage and practical accessibility of this storage capacity is uncertain and the availability of storage differs considerably across regions which can lead to broader socio-economic challenges of decarbonizing by CCS.

Alternate storage methods such as enhanced weathering, ocean fertilization, bioenergy with carbon capture and storage have not been considered in this work and may present additional opportunities [45].

S8. Changes to Direct Operating Costs (DOC) and comparison of biomass-derived SAF against PtL SAF and LH_2

We calculate the cost associated with the transition to a ZIA system based on a biomass-derived SAF in addition to the PtL SAF and LH_2 fuels presented in the main paper. We choose the hydroprocessed esters and fatty acids (HEFA) from waste fats, oils and grease (FOG) feedstock as the comparative biomass-derived SAF. We estimate the cost of producing HEFA FOG based jet fuel using a triangular distribution between 0.60 and 1.2 $/L jet A equivalent with a mode of 0.90 $/L based on the literature [45]. A lifecycle emissions index of 16.5 gCO_2e/MJ is assumed based on Staples et al [46] and is similar to the values reported under CORSIA [47].

Figure S13a shows that the change in direct operating costs for the HEFA FOG SAF is 11% higher than that of conventional aircraft fueled by jet A (compared to 22% higher for PtL SAF). The increase in direct operating costs of all three alternate fuels (HEFA FOG, PtL FOG and LH_2) are within 11-22% relative to conventional aircraft using jet A.

Figure S13b shows that the biomass-based SAF requires a greater reliance on atmospheric CO_2 removal since the fuel lifecycle GHG emissions of the HEFA FOG SAF are ~2.9 times that for the PtL SAF (see main paper).

While HEFA FOG based SAF has a cost advantage over PtL and LH_2 (which drives the lower societal costs) they are limited by feedstock availability [46] and may not be able to satisfy the energy demand of aviation.

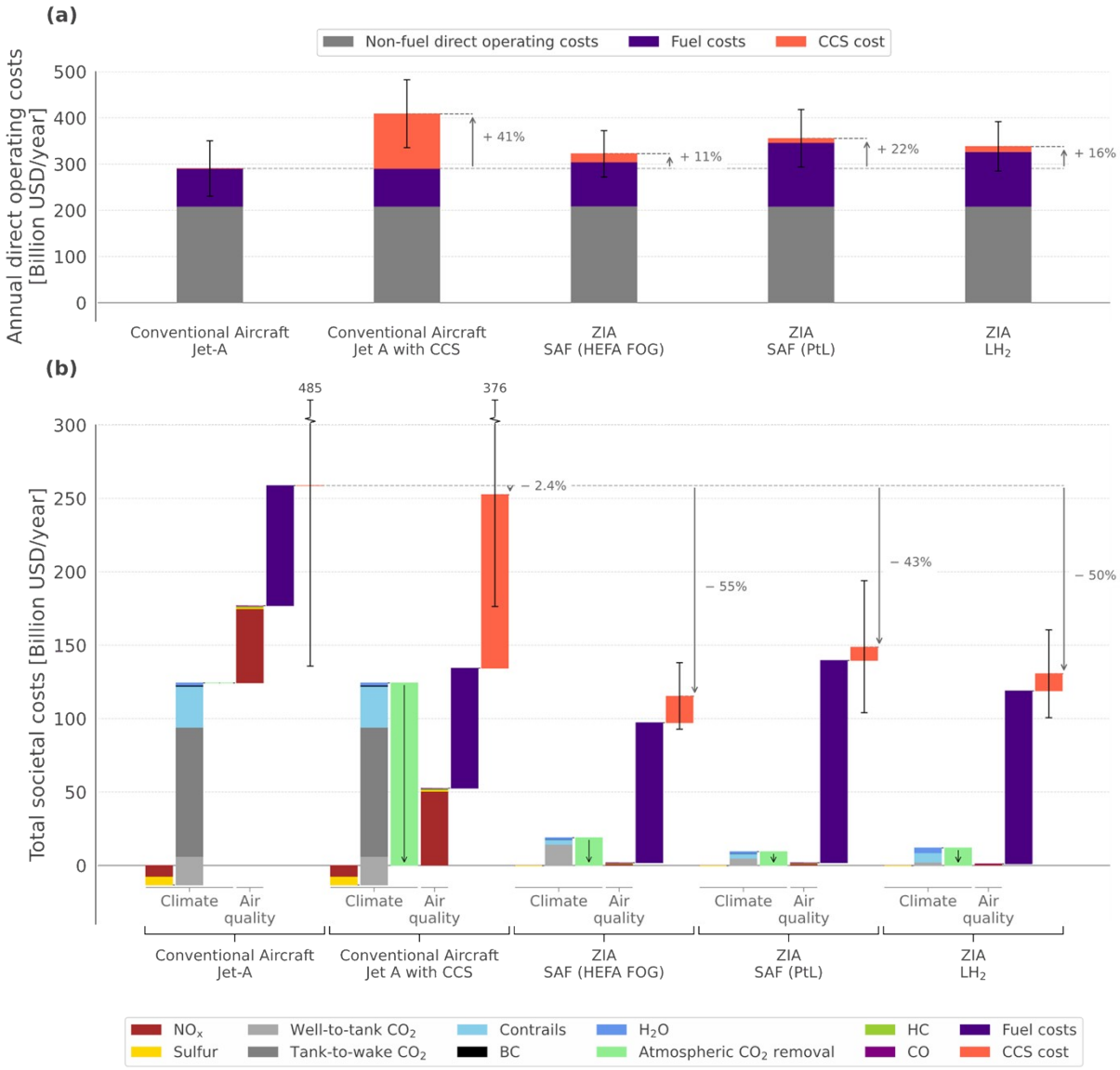

Figure S13: Annual direct operating costs (a) and total societal costs (b) in billions of USD for conventional aircraft fueled by jet A (with and without the use of CCS) as well as ZIA with different fuels. A HEFA FOG based SAF, a synthetic PtL SAF and LH_2 are shown.

Figure S14 below shows the annual direct operating costs (which consists of the cost associated with flying operations, maintenance, and depreciation and amortization of the aircraft capital cost) for the various systems considered here. In this work we have not quantified the change in aircraft research and development, manufacturing, or maintenance costs due to the LH_2 tanks, or PCEC systems. This will increase the non-fuel DOC (which is currently approximately evenly divided between labor, maintenance, and ownership costs). The first three scenarios shown: conventional aircraft using jet A fuel used in the present-day system, conventional aircraft with jet A fuel and CCS to have net-zero climate impacts, and conventional aircraft powered by the proposed PtL SAF with CCS, all have similar total societal costs. The ZIA systems can reduce the total societal cost by 43-50%.

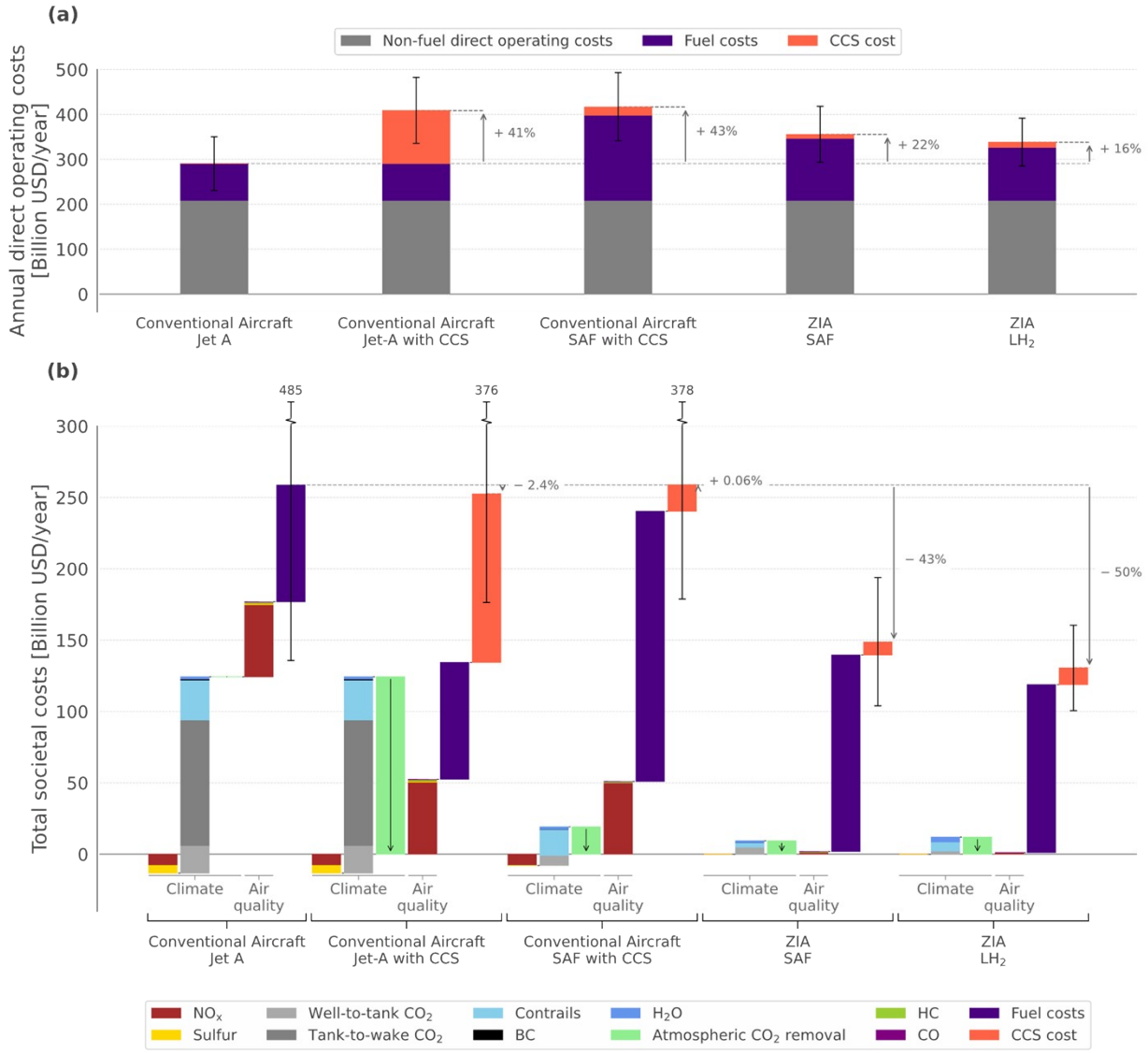

Figure S14: Cost of zero-impact air transport system in terms of (a) the direct operating costs per annum (includes the fuel and non-fuel direct operating costs, and the cost of CCS). Changes to non-fuel direct operating costs due to maintenance and staff etc. are not estimated and (b) total societal cost per annum (includes climate and air quality externalities, cost of fuel production and cost of required CCS). Conventional aircraft refers to the current fleet of B737s and A320s.

Advancements in sustainable alternate fuels for aviation have also resulted in "high-energy-density renewable jet fuel" with compositions such as reported by Rosenkoetter et al via the cycloaddition of isoprene [48]. They report an increase in specific energy of ~2.4% with respect to conventional Jet A. While innovations in fuel composition are important and can help improve the operational performance their impact on the net environmental costs in isolation is limited as calculated below.

As a sensitivity case we consider a fuel composition that results in a 10% decrease in mission fuel requirements (all else remaining constant, i.e., no redesign of the airplane and propulsion system this corresponds to an approximate 10% increase in the fuel specific energy relative to Jet

A). Assuming that the impact on contrails and other non-CO_2 impacts are negligible, we find that the use of the high-energy density fuel results in ~5% benefit relative to the baseline biomass based SAF with lower lifecycle GHG emissions as shown in Figure S15 below.

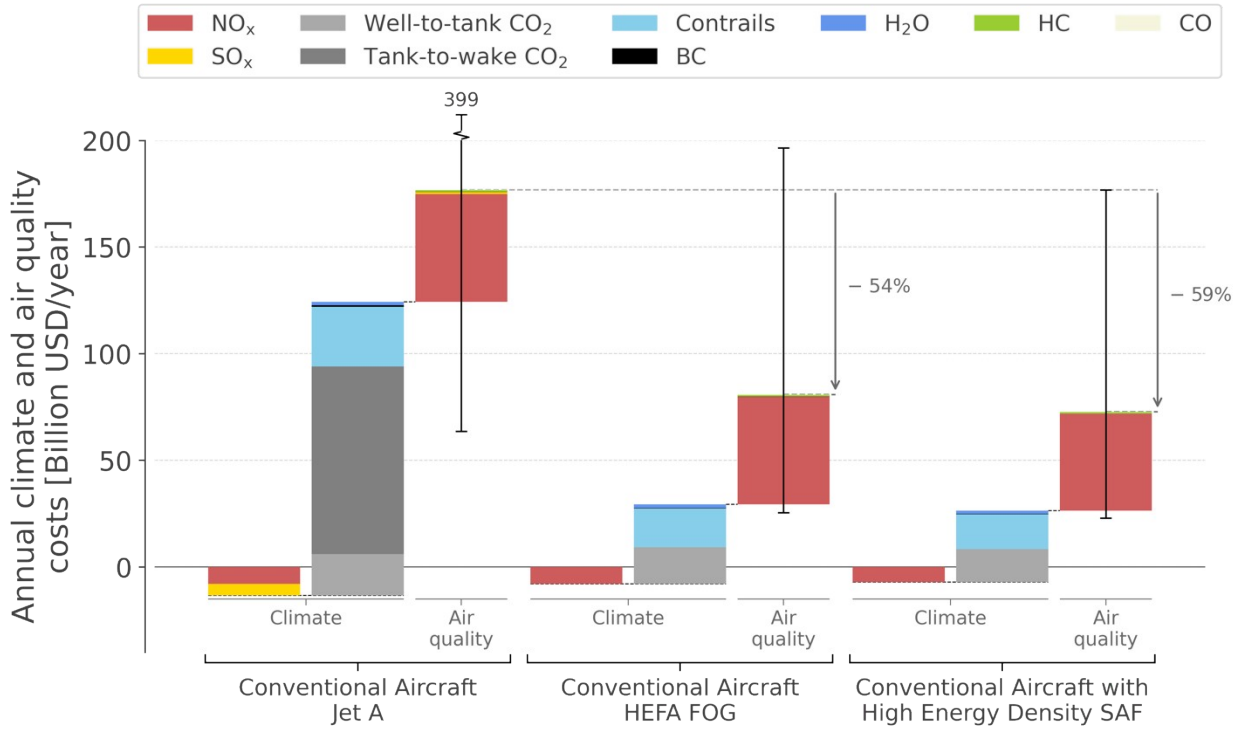

Figure S15: Environmental impact of advanced high-energy density drop-in SAF used in conventional present-day aircraft compared against the use of baseline SAF and Jet A fuels.

S9. Climate and air quality impact calculation

Climate impacts are quantified using Aviation environmental Portfolio Management Tool-Impacts Climate (APMT-IC) with three key updates to Grobler et al [49].

S9.1. Updates to APMT-IC

First, we update the contrail radiative forcing (RF) values with the recent aviation climate assessment in Lee et al [1]. We use a triangular uncertainty distribution with a minimum value of 20.9 mW/m^2, mid value of 69.78 mW/m^2, and upper bound of 118.62 mW/m^2 for the distance flown in 2006 based on the current literature [50–53]. The effective radiative forcing to radiative forcing (ERF/RF) ratio, which represents the temperature change per unit of forcing as compared to CO_2, is also adjusted by applying a triangular uncertainty distribution with a mid-value of 0.417, minimum value of 0.31 and maximum value of 0.59 based on results by Bickel et al [54], Ponater et al [55], and Rap et al [56].

The second update adjusts our NO_x-methane forcing pathway to additionally account for the additional impact of methane's short wave radiative forcing [1,57]. This results in a 14% reduction in our NO_x-methane net radiative forcing for the same quantity of NO_x emissions.

The third update aligns the estimated costs of global warming with more recent climate damages cost function from Howard and Sterner [58]. For a 2% discount rate and RCP2.6 and SSP2 background scenarios (that are consistent with a decarbonized future the estimated social cost of carbon in 2020 is 246 USD_{2020}/tonne of CO_2 (90% confidence interval 61.4 to 624). Similarly for a 3% discount rate, RCP4.5 and SSP1 the social cost of carbon in 2020 is 158 USD_{2020}/tonne CO_2 (90% confidence interval 46.4 to 352). This result is in line with recent global social cost of carbon estimates in literature, which range between 80 and 805 USD [59–61].

S9.2. Accounting for contrail radiative forcing from the use of LH_2 and SAF

Furthermore, to account for differences in contrail impacts from the combustion of SAF and LH_2 relative to conventional Jet A fuel we adapt the contrail forcing values in APMT-IC. These differences in contrail radiative forcing are due to changes in the water vapor emissions index, as well as the particle number emissions index. For SAF and LH_2 the water vapor emissions index is assumed to increase by a factor of 1.09 and 2.6 per unit fuel energy respectively [62,63] relative to Jet A. This increase in water vapor emissions increases the frequency of contrail formation, since the additional water vapor increases the range of atmospheric conditions (temperature and humidity) under which contrails can form [64,65]. Secondly, a decrease in particle emissions is also expected for both these fuels. For SAF, a 53% to 95% reduction in particle emissions is assumed based on the literature [66–69]. While zero particle emissions are expected from the use of LH_2, the presence of ambient particles (equivalent to10^{12} to 10^{13} per kilogram of fuel burned *(26)*) will result in the formation of contrails. Direct particle emissions (SAF scenario) and particles from ambient air (LH_2 scenario) form the nuclei on which the ice crystals condense. A change in particle number concentration therefore results in contrails with

fewer but larger ice crystals, which settle out to lower altitudes where it is warmer and evaporate faster. This decreases the optical depth and the lifetime of the contrail [62].

We account for the change in contrail radiative forcing in the ZIA-SAF and ZIA-LH_2 cases by applying a correction factor to the contrail RF of contrails formed while using conventional Jet A fuel based on the limited literature on the RF of LH_2 contrails. In order to capture the uncertainty in these studies we sample the correction factor from a distribution based on the literature that is then used in the Monte Carlo simulations in AMPT-IC.

In the ZIA-LH_2 case we use a triangular distribution with a central value of 0.85 (consistent with the central results of Marquart et al [70] and Ponater et al [55]) and lower and upper bound range of 0.1 to 1.6 (which captures the uncertainty range from Marquart et al [70] and Grewe et al [71]). Similarly for ZIA-SAF we use a triangular distribution with a central value of 0.58 and lower and upper bound range of 0.19 to 1.18 based on values from the literature [63,72,73]. Here we assume these adjustments can be made independently of the contrail avoidance estimation, but this independence has not been addressed in literature.

S9.3. Emissions

We derive fuel burn and emissions for the schedule file using the current fleet of the Boeing 737 and Airbus 320 aircraft. We do not forecast future flight schedules but use the current 2019 flight schedule for both the conventional present-day fleet as well as the proposed ZIA-LH_2 and ZIA-SAF fleet. Fuel burn for the conventional fleet is calculated with the Base of Aircraft Data (BADA) version 3.15 dataset. CO_2 and H_2O emissions are computed using emissions indices as listed in Brasseur et al [74]. Well-to-tank life-cycle CO_2 emissions are taken as 16 gCO_2e/MJ in line with ICAO CORSIA standard. Sulfur emissions are based on an assumed fuel sulfur content of 600 ppm. NO_x, carbon monoxide (CO), and unburned hydrocarbon (HC) emissions are derived using the Boeing fuel flow method 2 [75]. Soot emissions are derived using the FOX method [76].

Non-LTO fuel burn and emissions for the hydrogen aircraft are calculated using the aircraft design code and calculated as a function of flight level and aircraft mass. LTO fuel burn and NO_x emissions are derived following the same approach as conventional aircraft. Water vapor emissions are calculated assuming stoichiometric combustion, leading to 9 kgH_2O/kgH_2. Since hydrogen does not contain any fuel sulfur nor result in any carbon related emissions, the mass of SO_x, soot, CO, NMVOC, and CO_2 emissions are set to zero.

Fuel burn and NO_x emissions for the SAF aircraft are derived using the same methodology as the hydrogen aircraft. Here we assume soot emissions indices are between 4.9% and 47% of the conventional aircraft soot emissions based on the range in literature [66–69]. For CO and NMVOC we assume the same emissions indices as for conventional fuel. Water vapor emissions per unit mass are increased by a factor 1.11 to account for the additional hydrogen content of paraffinic jet fuel [63]. Since the carbon content of the PtL SAF consists entirely of atmospheric CO_2, the release of CO_2 during the direct (in-flight) combustion of the fuel is offset over its lifecycle. Therefore, the “tank-to-wake” (TTW) emissions for the ZIA-SAF and ZIA-LH_2 aircraft in Table S7 and S8 is zero. The “well-to-tank” (WTT) emissions are however not zero.

To ensure our reference cases and ZIA cases carry the same payload for the same distance, we adjust the emissions of the SAF and LH_2 aircraft cases to match the payload-distance product (seat-km) from the B737 and A320 schedule. This is necessary since the flights in the schedule occur on aircraft with between 100 and 240 seats, while the aircraft in this study have 220 seats each. This resulting adjustment factor is 0.766.

Table S7 shows the fleet level fuel burn and emissions for the aircraft considered in this work. The NO_x emissions are reduced by ~98%, and sulfur emissions are eliminated in the ZIA cases. The water vapor emissions from SAF are similar to that of the reference case (within 1.5%) the water vapor from the LH_2 aircraft is increased by a factor 2.6.

Table S8 shows the fleet wide fuel burn and emissions after accounting for contrail avoidance. These emissions results are used to calculate the climate and air quality impacts in the paper. We assume a LHV of 43.2 MJ/kg for Jet-A fuel and 44.1 MJ/kg for the SAF.

Table S7: Fuel burn and emissions from the different aircraft fleets without contrail avoidance. Here CO_2 emissions only account for fossil CO_2 emissions. *TTW is the tank-to-wake emissions and WTT is the well-to-tank emissions.

	Fuel burn [Tg]	Fuel energy [10^{12}MJ]	TTW* Fossil CO_2 [Tg]	H_2O [Tg]	NO_x [Tg]	Soot [Gg]	SO_x [Gg]	NM VOC [Gg]	CO [Gg]	WTT* fossil CO_2e [Tg]
Comparison: Jet-A B737 & A320	114	4.94	361	141	1.80	7.93	0.14	79.5	626	79.1
ZIA: SAF aircraft	80.7	3.56	0.00	111	0.040	1.48	0.00	57.3	451	20.2
ZIA: Hydrogen aircraft	33.4	4.01	0.00	301	0.039	0.00	0.00	0.00	0.00	9.2

Table S8: Contrail avoidance adjusted fuel burn and emissions from the different aircraft fleets. Here CO_2 emissions only account for fossil CO_2 emissions. *TTW is the tank-to-wake emissions and WTT is the well-to-tank emissions. The electricity demand is calculated based on the electric intensity of the fuel production pathways as shown in Table S4. The required land area is calculated using NREL reported average direct land area use for on-shore wind production based on data from the United States [77].

	Fuel burn [Tg]	Fuel energy [10^{12}MJ]	TTW* Fossil CO_2 [Tg]	H_2O [Tg]	NO_x [Tg]	Soot [Gg]	SO_2 [Gg]	NM VOC [Gg]	CO [Gg]	WTT* fossil CO_2e [Tg]	Electricity demand [TWh]	Required direct land area for wind [km^2]
Comparison: Jet-A B737 & A320	114	4.94	361	141	1.80	7.93	0.14	79.5	626	79.1	-	-
ZIA: SAF aircraft	81.6	3.60	0	112	0.040	1.50	0.000	58.0	456	20.4	2430	1910
ZIA: Hydrogen aircraft	33.8	4.05	0	304	0.040	0.00	0.00	0.00	0.00	9.3	1850	1460

S9.4. Air quality and climate impacts

Figure S16 shows the detailed contribution of various species to the climate and air quality impacts. Replacing the conventional aircraft in the target market with the ZIA-SAF and ZIA-LH_2 systems result in a 92% and 90% reduction in climate impact respectively. The ZIA-SAF and ZIA-LH_2 systems also result in a 96% and 98% reduction in air quality impact respectively.

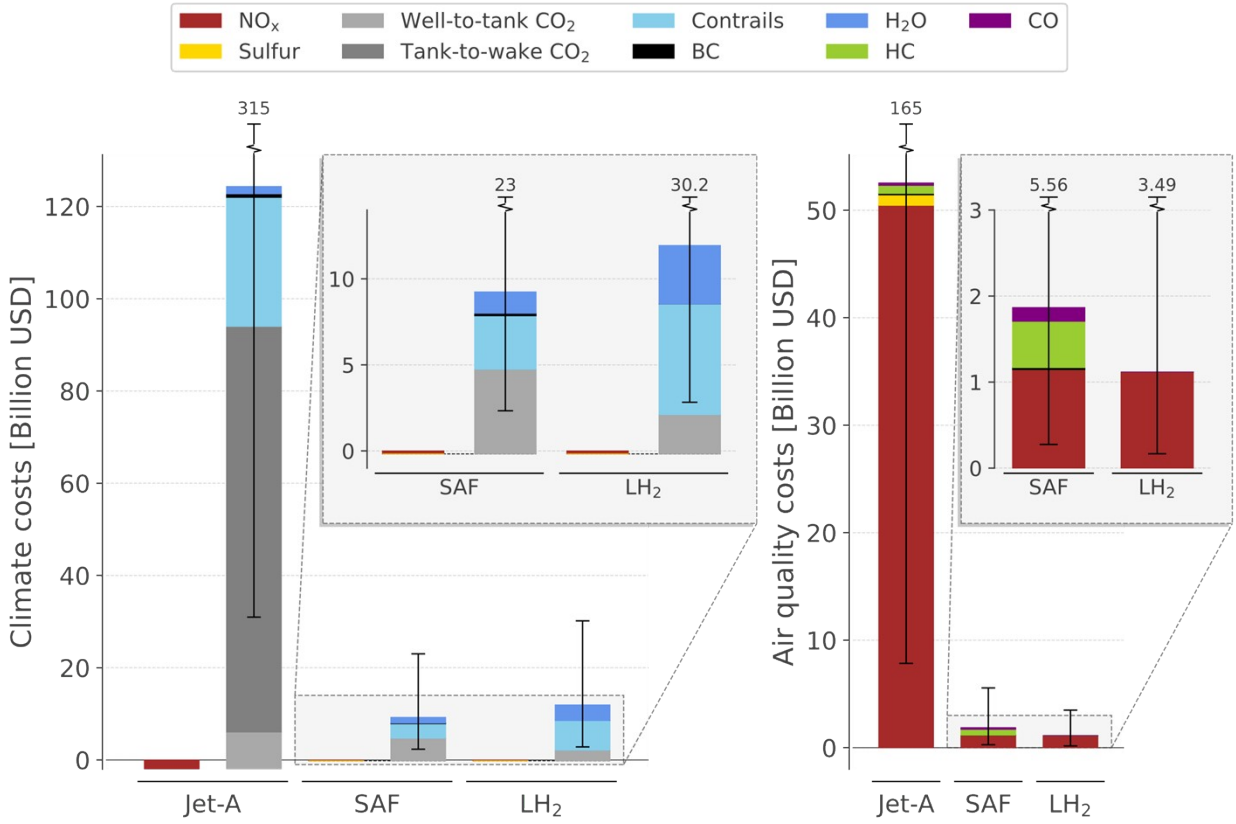

Figure S16: Detailed breakdown of climate and air quality impact for conventional aviation, ZIA-SAF and ZIA-LH_2 systems

S9.5. Sensitivity case: results for PV derived fuels

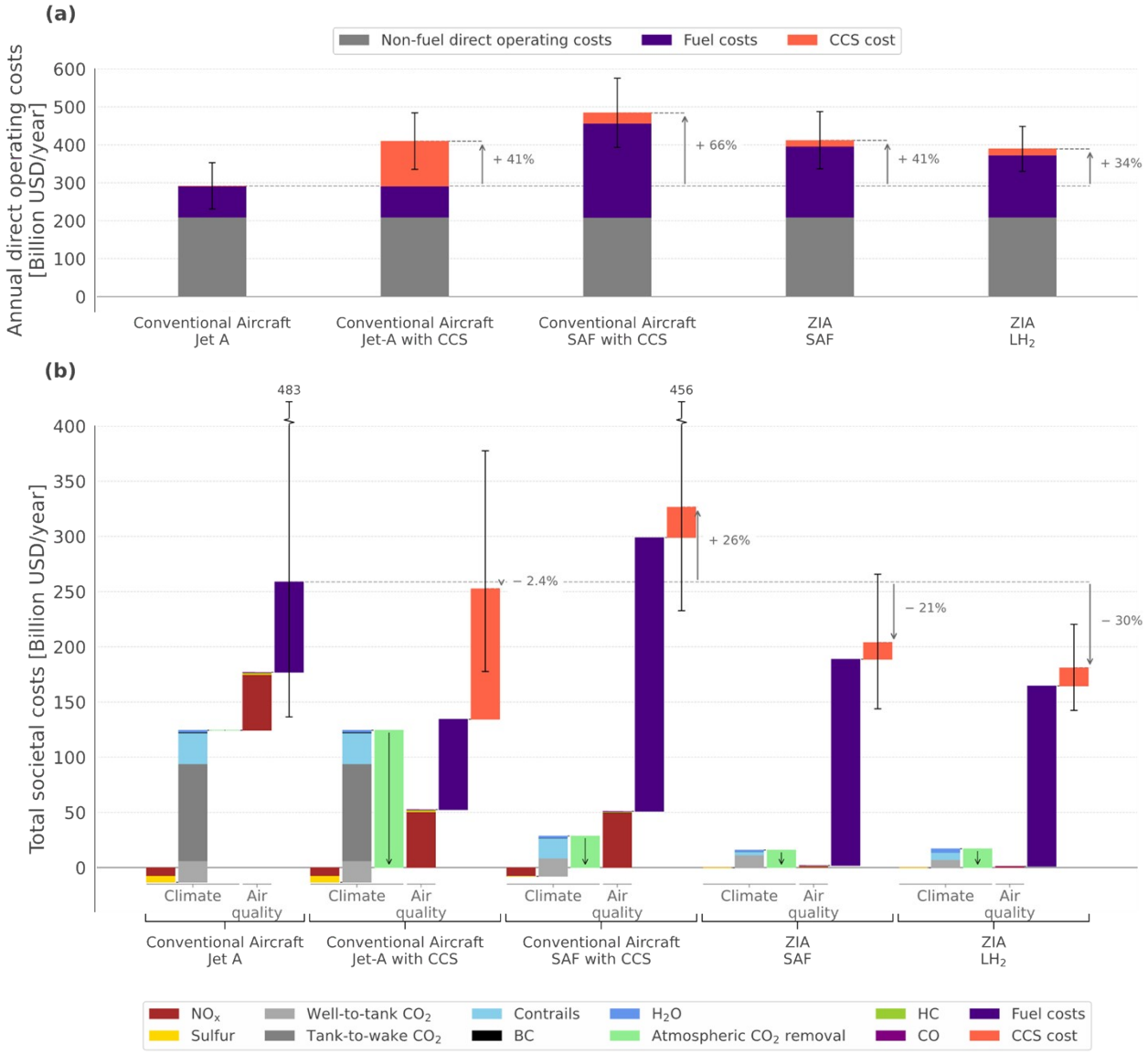

Figure S17: Changes in total societal impact factors for fuels derived using solar PV electricity.

S9.6. Sensitivity case: climate and air quality impacts for different discount rates

Figure S17 and S18 show the environmental costs (climate and air quality) for discount rates of 3% (Figure S17) and 7% respectively (Figure S18).

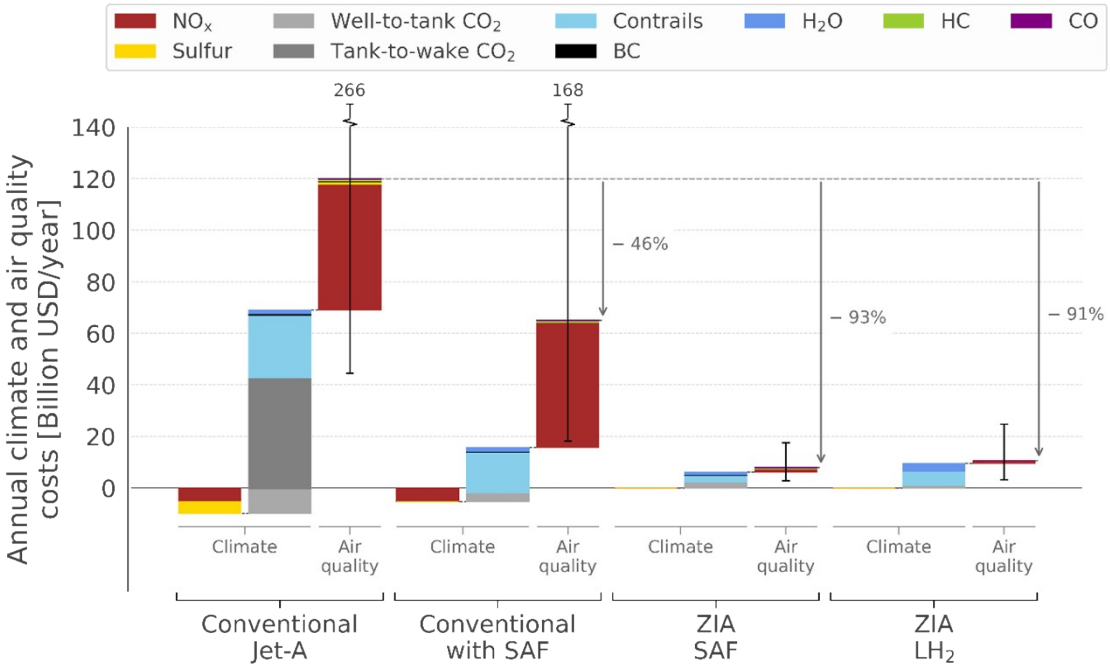

Figure S18: Climate and air quality impacts for a 3% discount rate

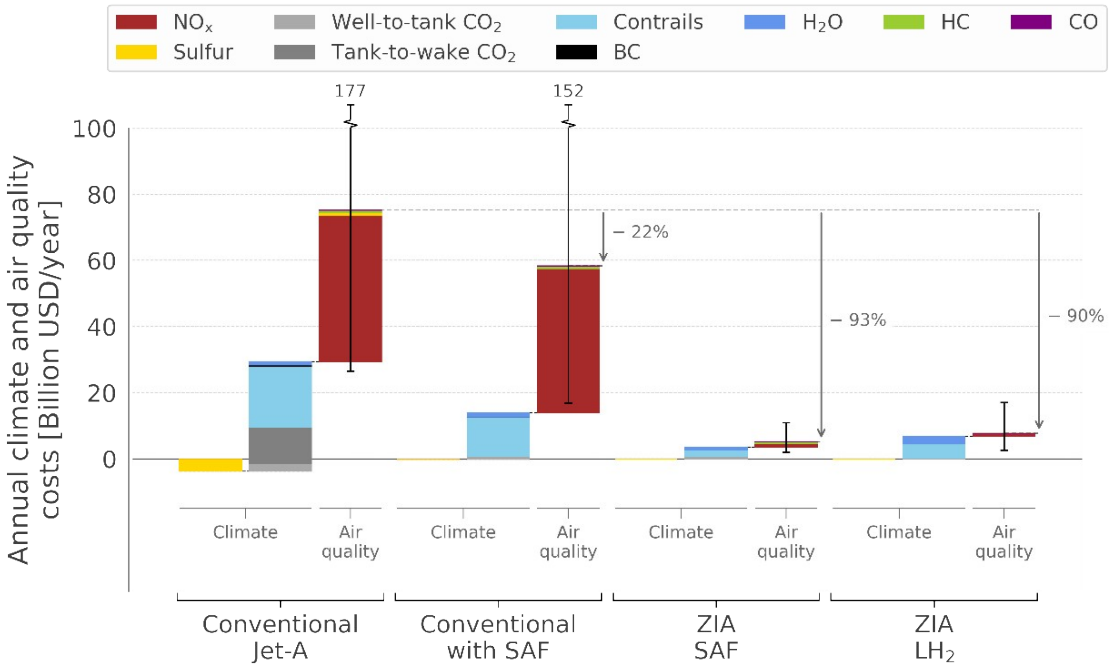

Figure S19: Climate and air quality impacts for a 7% discount rate

S10. Feasibility of ZIA systems under present day assumptions

The assumptions used in the main results show in the main text and above are based on the renewable energy (i.e., wind and solar based systems) assumptions detailed in Section S4. These values are based on the forecasts in 2050 and are as such uncertain. In this section we consider the sensitivity of our central results to factors external to today's aviation industry namely the LCOE and CF for energy production and the embodied emissions in the fuel production pathways. Tables S9 and S10 summarize the assumed values below.

Table S9: Cost assumptions used in quantifying the fuel production pathway costs based on present day assumptions for LCOE and CF.

			Units	Value		Source
				Advanced	Moderate	
Electricity generation	Photo-voltaic cells	LCOE	$/kWh	0.033	0.052	NREL ATB [3]
		CF	%	34	21	
	On-shore wind	LCOE	$/kWh	0.026	0.066	
		CF	%	50	26	

Table S10: Emission intensities of electricity generation and other processes, including embodied emissions. DAC plant embodied emissions shown are for with or without material recycling as reported by Deutz and Bardow [15] treated as upper and lower bounds here.

Process		Units	Value	Source
Electricity generation	Photo-voltaic cells	gCO_2e/kWh	44	Kim et al [16]
	On-shore wind	gCO_2e/kWh	4.4	Razdan and Garrett [17]
Electrolysis	PEM embodied emissions	gCO_2e/kgH_2	120	Bareiß et al [18]
Liquefaction	Liquefaction plant embodied emissions	gCO_2e/kgH_2	100	Assumed similar plant embodied emissions as Fuel conversion
CO_2 capture	DAC adsorbent emission intensity	$gCO_2e/kgCO_2$ captured	25	Deutz and Bardow [15]
	DAC plant embodied emissions	$gCO_2e/kgCO_2$ captured	[6.0, 16.0]	
Fuel conversion	Fischer-Tropsch and rWGS embodied emissions	gCO_2e/L jet fuel	60	Falter et al [8]
Electricity transport	HVDC construction embodied emissions	gCO_2e/kWh	2.5	Arvensen et al [19]

Figure S20 below shows the resulting cost and GHG emissions associated with the production of LH_2, and PtL SAF for the ZIA systems proposed in the main text. We find that the cost of producing the fuels under present day assumptions outlined above is approximately twice as high as year 2050 assumptions used in the main text (see Figure 1 of the main text) for a wind-based system. Furthermore, the associated GHG emissions under present day assumptions for a wind-based system are 14.3 gCO_2e/MJ for the PtL SAF (~83% reduction relative to Jet A) and 6.9 gCO_2e/MJ for LH_2 (~92% reduction relative to Jet A).

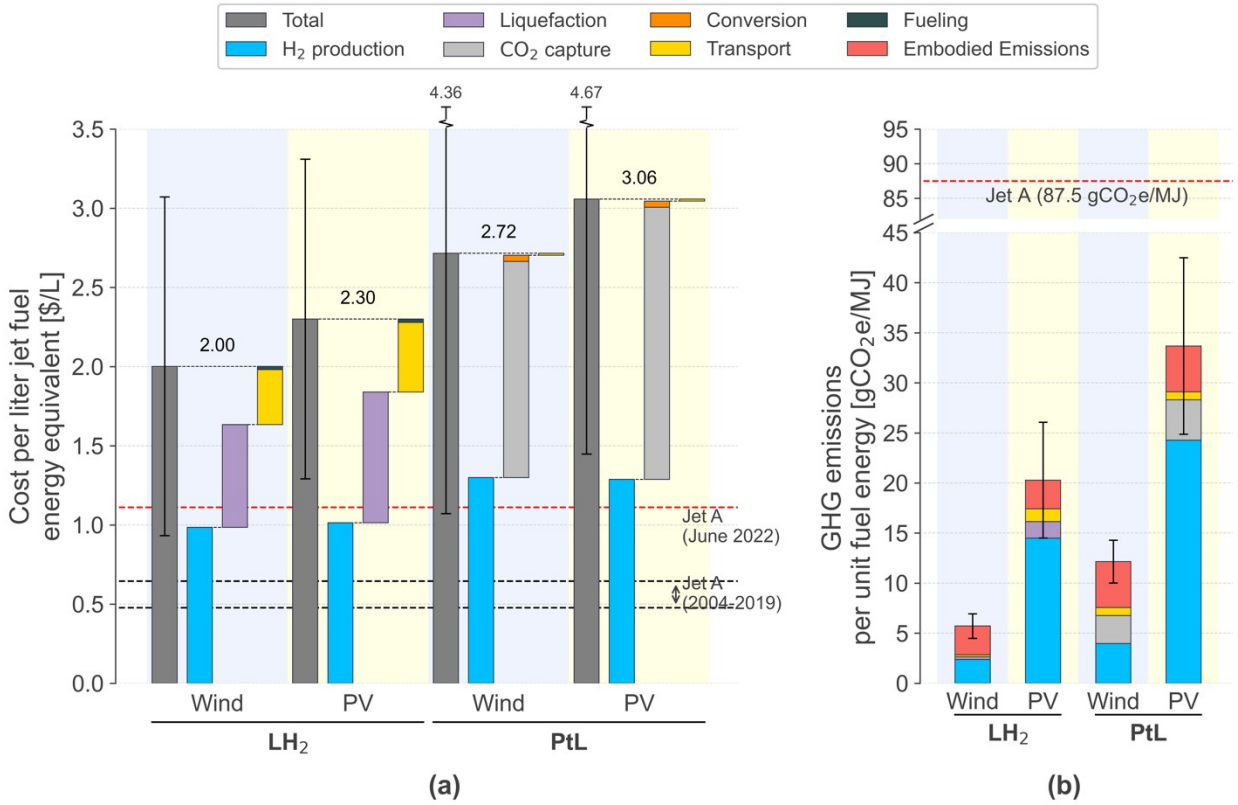

Figure S20: LH_2 and PtL SAF (a) costs in dollars per liter of jet fuel energy equivalent using present day (2021) LCOE and CF for wind and solar PV energy and (b) lifecycle GHG emissions in gCO_2e per MJ. Error bars represent the upper and lower bounds of costs and emissions that result from the technological and economic assumptions. Dashed black lines in panel (a) show the 2.5 – 97.5 percentile range of the jet A price from 2004-2019 and the dashed red line shows the price of jet A at time of writing. Embodied CO_2 in panel (b) represents the CO_2 emitted in the construction and setup of the process plants in each process.

We use the above calculations to quantify the change in total societal cost (sum of the monetized climate and air quality impacts, the cost of fuel, and CCS) associated with the ZIA system is 26% and 6% higher than the present-day system for the SAF and LH_2 systems respectively. The increase in societal cost is because the cost of CCS (mean cost of ~$545 per tonne of CO_2) and fuel costs (see Figure S20) outweigh the monetized benefit of near-zero climate and air quality impacts under these set of assumptions. This highlights the critical need for renewable energy to truly enable the near-zero impact systems detailed in the main text – including technology development and scale-up to reduce the LCOE of renewable energy in line with forecasts such as the NREL ATB for 2050.

References

[1] Lee D S, Fahey D W, Skowron A, Allen M R, Burkhardt U, Chen Q, Doherty S J, Freeman S, Forster P M, Fuglestvedt J, Gettelman A, De León R R, Lim L L, Lund M T, Millar R J, Owen B, Penner J E, Pitari G, Prather M J, Sausen R and Wilcox L J 2021 The contribution of global aviation to anthropogenic climate forcing for 2000 to 2018 *Atmospheric Environment* **244** 117834

[2] Myhre G, Shindell D, Bréon F-M, Collins W, Fuglestvedt J, Huang J, Koch D, Lamarque J, Lee D, Mendoza B, Nakajima T, Robock A, Stephens G, Takemura T, Zhang H, Qin D, Plattner G, Tignor M, Allen S, Boschung J, Nauels A, Xia Y, Bex V and Midgley P 2013 *Anthropogenic and Natural Radiative Forcing. In: Climate Change 2013: The Physical Science Basis. Contribution of Working Group I to the Fifth Assessment Report of the Intergovernmental Panel on Climate Change* (Cambridge United Kingdom and New York, NY, USA: Cambridge University Press)

[3] Vimmerstedt L 2022 2022 Annual Technology Baseline (ATB) Cost and Performance Data for Electricity Generation Technologies ed T Stehly

[4] Abel J and Allroggen F 2023 Global Costs and Infrastructure Requirements for LH2Airport Refueling *AIAA AVIATION 2023 Forum* AIAA AVIATION Forum (American Institute of Aeronautics and Astronautics)

[5] International Air Transport Association (IATA) 2015 Economic Performance of the Airline Industry

[6] Mayyas A T, Ruth M F, Pivovar B S, Bender G and Wipke K B 2019 *Manufacturing Cost Analysis for Proton Exchange Membrane Water Electrolyzers* (United States)

[7] Hanna R, Abdulla A, Xu Y and Victor D G 2021 Emergency deployment of direct air capture as a response to the climate crisis *Nature Communications* **12**

[8] Falter C, Valente A, Habersetzer A, Iribarren D and Dufour J 2020 An integrated techno-economic, environmental and social assessment of the solar thermochemical fuel pathway *Sustainable Energy & Fuels* **4** 3992–4002

[9] d'Amore-Domenech R, Meca V L, Pollet B G and Leo T J 2023 On the bulk transport of green hydrogen at sea: Comparison between submarine pipeline and compressed and liquefied transport by ship *Energy* **267** 126621

[10] Saadi F H, Lewis N S and McFarland E W 2018 Relative costs of transporting electrical and chemical energy *Energy Environ. Sci.* **11** 469–75

[11] Anon EIA - Assessing HVDC Transmission for Impacts of Non-Dispatchable Generation

[12] International Energy Agency 2019 *The Future of Hydrogen: Seizing today's opportunities* (OECD)

[13] Aasadnia M and Mehrpooya M 2018 Large-scale liquid hydrogen production methods and approaches: A review *Applied Energy* **212** 57–83

[14] ICAO Committee on Aviation Environmental protection (CAEP). 2022 *Report on the feasibility of a long-term aspirational goal (LTAG) for international civil aviation CO2 emission reductions* (International Civil Aviation Organization)

[15] Deutz S and Bardow A Life-cycle assessment of an industrial direct air capture process based on temperature-vacuum swing adsorption

[16] Kim H C, Fthenakis V, Choi J-K and Turney D E 2012 Life Cycle Greenhouse Gas Emissions of Thin-film Photovoltaic Electricity Generation *Journal of Industrial Ecology* **16** S110–21

[17] Razdan P and Garrett P 2019 *Life Cycle Assessment of electricity production from an onshore V150-4.2 MW wind plant* (Denmark: Vestas)

[18] Bareiß K, de la Rua C, Möckl M and Hamacher T 2019 Life cycle assessment of hydrogen from proton exchange membrane water electrolysis in future energy systems *Applied Energy* **237** 862–72

[19] Arvesen A, Nes R N, Huertas-Hernando D and Hertwich E G 2014 Life cycle assessment of an offshore grid interconnecting wind farms and customers across the North Sea *Int J Life Cycle Assess* **19** 826–37

[20] Drela M 2011 Development of the D8 Transport Configuration *29th AIAA Applied Aerodynamics Conference* 27–30

[21] Greitzer E M, Bonnefoy P A, De La Rosa Blanco E, Dorbian C S, Drela M, Hall D K, Hansman R J, Hileman J I, Liebeck R H, Lovegren J, Mody P, Pertuze J a., Sato S, Spakovszky Z S, Tan C S and Hollman J S 2010 N + 3 Aircraft Concept Designs and Trade Studies , Final Report Volume 1 **1** 1–187

[22] Mital S K, Gyekenyesi J Z, Arnold S M, Sullivan R M, Manderscheid J M and Murthy P L N 2006 *Review of Current State of the Art and Key Design Issues With Potential Solutions for Liquid Hydrogen Cryogenic Storage Tank Structures for Aircraft Applications* (National Aeronautics and Space Administration)

[23] Winnefeld C, Kadyk T, Bensmann B, Krewer U and Hanke-Rauschenbach R 2018 Modelling and Designing Cryogenic Hydrogen Tanks for Future Aircraft Applications *Energies* **11** 105

[24] Brewer G D 1991 *Hydrogen aircraft technology* (Boca Raton: CRC Press)

[25] Barron R F 1985 *Cryogenic systems* (New York : Oxford [Oxfordshire]: Oxford University Press ; Clarendon Press)

[26] Verstraete D 2009 *The Potential of Liquid Hydrogen for long range aircraft propulsion* (United Kingdom: Cranfield University)

[27] Dowdle A, Hall D K and Lang J 2018 Electric Propulsion Architecture Assessment via Signomial Programming *2018 AIAA/IEEE Electric Aircraft Technologies Symposium* 1–23

[28] Ofori-Tenkorang J 1996 *Permanent-magnet synchronous motors and associated power electronics for direct-drive vehicle propulsion* Thesis (Massachusetts Institute of Technology)

[29] Hall D K, Greitzer E M, Dowdle A P, Gonzalez J J, Hoburg W W, Lang J H, Sabnis J S, Spakovszky Z S, Yutko B, Courtin C, Thalheimer W, Trollinger L, Tylko J, Varney N, Uranga A, Byahut S and Kruger M 2019 *Feasibility of Electrified Propulsion for Ultra-Efficient Commercial Aircraft Final Report*

[30] Sagerser D A, Lieblein S and Krebs R P 1971 *Empirical expressions for estimating length and weight of axial-flow components of VTOL powerplants*

[31] Jansen R, Bowman C, Jankovsky A, Dyson R and Felder J 2017 Overview of NASA Electrified Aircraft Propulsion (EAP) Research for Large Subsonic Transports *53rd AIAA/SAE/ASEE Joint Propulsion Conference* AIAA Propulsion and Energy Forum (American Institute of Aeronautics and Astronautics)

[32] Prashanth P, Speth R L, Eastham S D, Sabnis J S and Barrett S R H H 2021 Post-combustion emissions control in aero-gas turbine engines *Energy & Environmental Science* **14** 916–30

[33] Tronconi E and Forzatti P 1992 Adequacy of lumped parameter models for SCR reactors with monolith structure *AIChE Journal* **38** 201–10

[34] Tronconi E 1997 Interaction between chemical kinetics and transport phenomena in monolithic catalysts *Catalysis Today* **34** 421–7

[35] Gao H 2013 *Aircraft cruise phase altitude optimization considering contrail avoidance* Thesis (Massachusetts Institute of Technology)

[36] Noppel F, Singh R and Taylor M 2012 Contrail and Cirrus Cloud Avoidance 25th Congress of the International Council of the Aeronautical Sciences

[37] Sridhar B, Ng H K and Chen N Y 2011 Aircraft Trajectory Optimization and Contrails Avoidance in the Presence of Winds *Journal of Guidance, Control, and Dynamics* **34** 1577–84

[38] Sridhar B, Ng H K and Chen N 2012 Uncertianty Quantification in the Development of Aviation Operations to Reduce Aviation Emissions and Contrails 28th Congress of the International Council of the Aeronautical Sciences

[39] Yin F, Grewe V, Frömming C and Yamashita H 2018 Impact on flight trajectory characteristics when avoiding the formation of persistent contrails for transatlantic flights *Transportation Research Part D: Transport and Environment* **65** 466–84

[40] Klima K 2005 *Assessment of a global contrail modeling method and operational strategies for contrail mitigation* Thesis (Massachusetts Institute of Technology)

[41] de Coninck H, Revi A, Babiker M, Bertoldi P, Buckeridge M, Cartwright A, Dong W, Ford J, Fuss S and Hourcade J-C 2018 *Strengthening and implementing the global response. Global Warming of 1.5C an IPCC special report.*

[42] Metz B, Davidson O, de Coninck H, Loos M and Meyer L 2005 *Carbon Dioxide Capture and Storage — IPCC* (Cambridge: IPCC)

[43] Kearns J, Teletzke G, Palmer J, Thomann H, Kheshgi H, Chen Y-H H, Paltsev S and Herzog H 2017 Developing a Consistent Database for Regional Geologic CO2 Storage Capacity Worldwide *Energy Procedia* **114** 4697–709

[44] IEA 2021 The world has vast capacity to store CO2: Net zero means we'll need it *IEA*

[45] Wang Z J, Staples M D, Tyner W E, Zhao X, Malina R, Olcay H, Allroggen F and Barrett S R H 2021 Quantitative Policy Analysis for Sustainable Aviation Fuel Production Technologies *Frontiers in Energy Research* **9**

[46] Staples M D, Malina R, Suresh P, Hileman J I and Barrett S R H 2018 Aviation CO2 emissions reductions from the use of alternative jet fuels *Energy Policy* **114** 342–54

[47] International Civil Aviation Organization 2021 *CORSIA Default Life Cycle Emissions Values for CORSIA Eligible Fuels* (International Civil Aviation Organization)

[48] Rosenkoetter K E, Kennedy C R, Chirik P J and Harvey B G 2019 [4 + 4]-cycloaddition of isoprene for the production of high-performance bio-based jet fuel *Green Chem.* **21** 5616–23

[49] Grobler C, Wolfe P J, Dasadhikari K, Dedoussi I C, Allroggen F, Speth R L, Eastham S D, Agarwal A, Staples M D, Sabnis J and Barrett S R H 2019 Marginal climate and air quality costs of aviation emissions *Environ. Res. Lett.* **14** 114031

[50] Burkhardt U and Kärcher B 2011 Global radiative forcing from contrail cirrus *Nature Clim Change* **1** 54–8

[51] Bock L and Burkhardt U 2016 Reassessing properties and radiative forcing of contrail cirrus using a climate model *Journal of Geophysical Research: Atmospheres* **121** 9717–36

[52] Schumann U, Penner J E, Chen Y, Zhou C and Graf K 2015 Dehydration effects from contrails in a coupled contrail–climate model *Atmospheric Chemistry and Physics* **15** 11179–99

[53] Chen C-C and Gettelman A 2013 Simulated radiative forcing from contrails and contrail cirrus *Atmospheric Chemistry and Physics* **13** 12525–36

[54] Bickel M, Ponater M, Bock L, Burkhardt U and Reineke S 2020 Estimating the Effective Radiative Forcing of Contrail Cirrus *Journal of Climate* **33** 1991–2005

[55] Ponater M, Pechtl S, Sausen R, Schumann U and Hüttig G 2006 Potential of the cryoplane technology to reduce aircraft climate impact: A state-of-the-art assessment *Atmospheric Environment* **40** 6928–44

[56] Rap A, Forster P M, Haywood J M, Jones A and Boucher O 2010 Estimating the climate impact of linear contrails using the UK Met Office climate model *Geophysical Research Letters* **37**

[57] Etminan M, Myhre G, Highwood E J and Shine K P 2016 Radiative forcing of carbon dioxide, methane, and nitrous oxide: A significant revision of the methane radiative forcing *Geophysical Research Letters* **43** 12,614-12,623

[58] Howard P H and Sterner T 2017 Few and Not So Far Between: A Meta-analysis of Climate Damage Estimates *Environ Resource Econ* **68** 197–225

[59] Pindyck R S 2019 The social cost of carbon revisited *Journal of Environmental Economics and Management* **94** 140–60

[60] Hänsel M C, Drupp M A, Johansson D J A, Nesje F, Azar C, Freeman M C, Groom B and Sterner T 2020 Climate economics support for the UN climate targets *Nat. Clim. Chang.* **10** 781–9

[61] Ricke K, Drouet L, Caldeira K and Tavoni M 2018 Country-level social cost of carbon *Nature Clim Change* **8** 895–900

[62] Gierens K, Lim L and Eleftheratos K 2008 A Review of Various Strategies for Contrail Avoidance *TOASCJ* **2** 1–7

[63] Caiazzo F, Agarwal A, Speth R L and Barrett S R H 2017 Impact of biofuels on contrail warming *Environ. Res. Lett.* **12** 114013

[64] Gierens K and Spichtinger P 2000 On the size distribution of ice-supersaturated regions in the upper troposphere and lowermost stratosphere *Annales Geophysicae* vol 18 (Springer) pp 499–504

[65] Kärcher B 2018 Formation and radiative forcing of contrail cirrus *Nat Commun* **9** 1824

[66] Moore R H, Thornhill K L, Weinzierl B, Sauer D, D'Ascoli E, Kim J, Lichtenstern M, Scheibe M, Beaton B, Beyersdorf A J, Barrick J, Bulzan D, Corr C A, Crosbie E, Jurkat T, Martin R, Riddick D, Shook M, Slover G, Voigt C, White R, Winstead E, Yasky R, Ziemba L D, Brown A, Schlager H and Anderson B E 2017 Biofuel blending reduces particle emissions from aircraft engines at cruise conditions *Nature* **543** 411–5

[67] Voigt C, Kleine J, Sauer D, Moore R H, Bräuer T, Le Clercq P, Kaufmann S, Scheibe M, Jurkat-Witschas T, Aigner M, Bauder U, Boose Y, Borrmann S, Crosbie E, Diskin G S, DiGangi J, Hahn V, Heckl C, Huber F, Nowak J B, Rapp M, Rauch B, Robinson C, Schripp T, Shook M, Winstead E, Ziemba L, Schlager H and Anderson B E 2021 Cleaner burning aviation fuels can reduce contrail cloudiness *Commun Earth Environ* **2** 1–10

[68] Speth R L, Rojo C, Malina R and Barrett S R H 2015 Black carbon emissions reductions from combustion of alternative jet fuels *Atmospheric Environment* **105** 37–42

[69] Beyersdorf A J, Timko M T, Ziemba L D, Bulzan D, Corporan E, Herndon S C, Howard R, Miake-Lye R, Thornhill K L, Winstead E, Wey C, Yu Z and Anderson B E 2014 Reductions in aircraft particulate emissions due to the use of Fischer–Tropsch fuels *Atmospheric Chemistry and Physics* **14** 11–23

[70] Marquart S, Ponater M, Strö m L and Gierens K 2005 An upgraded estimate of the radiative forcing of cryoplane contrails *metz* **14** 573–82

[71] Grewe V, Bock L, Burkhardt U, Dahlmann K, Gierens K, Hüttenhofer L, Unterstrasser S, Rao A G, Bhat A, Yin F, Reichel T G, Paschereit O and Levy Y 2017 Assessing the climate impact of the AHEAD multi-fuel blended wing body *Meteorologische Zeitschrift* 711–25

[72] Burkhardt U, Bock L and Bier A 2018 Mitigating the contrail cirrus climate impact by reducing aircraft soot number emissions *npj Clim Atmos Sci* **1** 1–7

[73] Teoh R, Schumann U, Majumdar A and Stettler M E J 2020 Mitigating the Climate Forcing of Aircraft Contrails by Small-Scale Diversions and Technology Adoption *Environ. Sci. Technol.* **54** 2941–50

[74] Brasseur G P, Gupta M, Anderson B E, Balasubramanian S, Barrett S, Duda D, Fleming G, Forster P M, Fuglestvedt J, Gettelman A, Halthore R N, Jacob S D, Jacobson M Z, Khodayari A, Liou K-N, Lund M T, Miake-Lye R C, Minnis P, Olsen S, Penner J E, Prinn R, Schumann U, Selkirk H B, Sokolov A, Unger N, Wolfe P, Wong H-W, Wuebbles D W, Yi B, Yang P and Zhou C 2016 Impact of Aviation on Climate: FAA's Aviation Climate Change Research Initiative (ACCRI) Phase II *Bulletin of the American Meteorological Society* **97** 561–83

[75] DuBois D and Paynter G C 2006 "Fuel Flow Method2" for Estimating Aircraft Emissions *SAE Technical Papers*

[76] Stettler M E J, Boies A M, Petzold A and Barrett S R H 2013 Global Civil Aviation Black Carbon Emissions *Environ. Sci. Technol.* **47** 10397–404

[77] Denholm P, Hand M, Jackson M and Ong S 2009 *Land Use Requirements of Modern Wind Power Plants in the United States*